



**Improved Nuclear Site characterization for waste minimization
in DD operations under constrained Environment**

Research and Innovation action
NFRP-2016-2017-1

**Statistical approach guide
- UC3b Annex -
Deliverable D3.7**

Version n° 1

Authors: Y. Desnoyers (Geovariances), N. Pérot (CEA)

<http://insider-h2020.eu/>



*This project has received funding from the Euratom research and training programme 2014-2018 under the grant agreement n°755554 .
The content in this deliverable reflects only the author(s)'s views. The European Commission is not responsible for any use that may be made of the information it contains.*



Document Information

Grant Agreement #: 755554

Project Title: Improved Nuclear Site characterization for waste minimization in DD operations under constrained Environment

Project Acronym: INSIDER

Project Start Date: 01 June 2017

Related work package: WP 3: Sampling strategy

Related task(s):

Lead Organisation: Geovariances

Submission date:

Dissemination Level: Confidential

History

Date	Submitted by	Reviewed by	Version (Notes)

Table of contents

List of Tables	3
List of Figures	3
Summary	6
1 Annex 4: UC3b Summary	7
1.1 Overall strategy.....	7
1.2 Data analysis & sampling design	8
1.3 References	42

List of Tables

Table 1. Acquired samples through graphite of G2 reactor, after shutdown [2].	8
Table 2: Number of available data and variation range of measurement uncertainties for the 13 studied radionuclides.	18
Table 3: Difference on total activity of ³⁶ Cl estimated by statistical models without uncertainty treatment and with uncertainty treatment.	20
Table 4. Number of imported samples, separated by radionuclide and core name.....	22
Table 5. Dispersion of average of variances.	30
Table 6. Graphite volume, exceeding the selected threshold for C-14, corresponding to the accepted risk (Figure 39a).....	42
Table 7. Inventory of C-14 corresponding to the accepted risk (Figure 39b).....	42

List of Figures

Figure 1 : General representation of the graphite volume from G2 reactor (Assystem EOS).	7
Figure 2. Location of graphite samples acquired from the moderator or reflector.	8
Figure 3. Sampling, subsampling and duplicate analyses in horizontal and vertical cores (a), also in channels (b).	9
Figure 4. Searching duplicate activities of horizontal and vertical core, according to six characteristics: (i) core type, (ii) sampled interval in the core, (iii) subsample name, (iv) subsample mass, (v) radionuclide and (vi) activity date. Microsoft Access software is used. .	10
Figure 5. Comparing reported and calculated log10 average of duplicates (a). Coefficient of variation of duplicates versus the log10 average (b). Average of coefficient of variation in each radionuclide (c).	11
Figure 6. Comparing the weighted log10 average of subsamples and their log10 standard deviation (a). Average of coefficient of variation in each radionuclide (b).	12
Figure 7. Searching types in channels, according to three characteristics: (i) channel position, (ii) sampled interval in the channel and (iii) radionuclide. Microsoft Access software is used.	13
Figure 8. Comparing the reported and calculated log10 average of type pairs activity (a). Comparing the weighted log10 average of type pairs and their log10 standard deviation (b). Average of coefficient of variation in each radionuclide (c).	13
Figure 9. Profile of activity of radionuclides in the vertical core of the G2 reactor graphite, according to the analysis protocol: SPR Marcoule 1989 in purple, LARC MA in pink, Leaching 2004 in blue.	14
Figure 10. Comparing log10 measured activity by protocols LARC MA and SPR Marcoule 1989 for the samples with the maximum distance of 20 cm (a). Comparing the log10 measured activity	



by protocols leaching 2004 and SPR Marcoule 1980 for the sample V36 at 15.4 m on the vertical core (b). Comparing coefficient of variation of measurement protocols for of each radionuclide (c). 15

Figure 11. Comparing reported average of tritium (H-3) activity by two methods A1 and B2 (a). Comparing reported and calculated average of duplicates of H-3 (b). 16

Figure 12. Comparing dispersions between core duplicates, between core subsamples and between channel types. 17

Figure 13 : Dispersion of measurement data for ³⁶Cl according radial coordinate with two identified outliers on left (a) and without outliers on right (b). 18

Figure 14: Histograms for ³⁶Cl activities on left (a) and for relative uncertainty measurements on right (b). 19

Figure 15: Activity and uncertainty measurements for ³⁶Cl according to axe distance and quantile curves for statistical models without uncertainty treatment on left (a) and with uncertainty treatment on right (b). 19

Figure 16: Graphical representation of activity repartition of ³⁶Cl estimated by the statistical model with uncertainty treatment with median on left (a) and 90%-quantile on right (b). 20

Figure 17 : Lognormal distribution law fitted without uncertainty treatment on left (a) and with uncertainty treatment on right (b) for activity measurement data of ¹³³Ba. 20

Figure 18 : 95% confidence intervals estimated by CARTOSTAT methodology and by activation simulations. 21

Figure 19 : Relative differences between median estimations without and with uncertainty treatment. 21

Figure 20. Histograms of the nine radionuclides in the graphite of G2 reactor. 23

Figure 21. Cross-plots of activity of radionuclide C-14 versus H-3, Cl-36, Co-60 and Cs-137. Besides, Cl-36 versus Eu-154 and Eu-155 in the graphite of G2 reactor. 24

Figure 22. Comparing coefficient of variation (CV) of samples (global) with average of coefficient of variation of subsamples, duplicates and types. 25

Figure 23. Profiles of activity of radionuclides (LARC MA protocol) in the G2 reactor graphite: vertical core (a), horizontal core (b), channels W14P (c) and W17A (d) 27

Figure 24. Experimental variograms of nine radionuclides in the graphite of G2 reactor. 29

Figure 25. Variogram modelling of C-14 activity in the graphite of G2 reactor. Anisotropic spherical function is used. 29

Figure 26. Sampling, subsampling and duplicate analysis. 30

Figure 27. Variance dispersion of C-14. 31

Figure 28. Imported duplicates and samples (a) and histogram of duplicates (b). 31

Figure 29. Directional experimental variograms of C-14 duplicates. 32

Figure 30. Accumulation (inventory) of C-14. 33

Figure 31. Local risk of C-14 in the graphite of G2 reactor. Probability of exceeding an arbitrary chosen threshold for C-14: a) Vertical East-West section at the location of about the vertical core. b) Vertical North-South section at location of about the vertical core. c) 3D view of cells with 95% probability of exceeding the arbitrary threshold of C-14. 36

Figure 32. Classification curve of graphite volumes from G2 reactor with activity higher than the arbitrary chosen threshold of C-14. 37

Figure 33. Grid blocks of moderator of graphite. Back reflector is ignored. 37

Figure 34. Variability of C-14 in different directions, modelled by regression models. 38

Figure 35. Regression-based model of C-14 in the moderator of graphite core. 39

Figure 36. Cross-plot of regression-based C-14 versus sample-based C-14. 39



Figure 37. Local risk of C-14 in the graphite of G2 reactor. Probability of exceeding the selected threshold, calculated by simple simulation (two sections on left) and co-simulation (two sections on right). The main variable (C-14 samples) are also shown..... 40

Figure 38. Histograms of probability of exceeding the threshold, calculated by simulation (a) and co-simulation (b), and cross-plot of them (c). 41

Figure 39. Global risk of C-14 in the graphite of G2 reactor: a) Volume of the graphite of G2 reactor with activity higher than the selected threshold for C-14. b) Accumulation (inventory) of C-14. The curves of simple simulation (TBS) and co-simulation (Co-TBS) are compared..... 41

Summary

The INSIDER project (2017-2021) developed and validated a new and improved integrated characterization methodology and strategy during nuclear decommissioning and dismantling operations of nuclear power plants, post-accidental land remediation or nuclear facilities under constrained environments.

One significant part of this project was the implementation on several application cases. This paper is dedicated to the radiological characterization for use case 3b (UC3b) dealing with activated graphite. For this application case, the constraint environment comes from the difficulty to collect measurements and samples in the reactor on the one hand and the fact that samples were collected in the past with no possibility for additional investigations within the INSIDER framework. This task has been initiated by gathering prior knowledge for the activated materials and analysing the available dataset (historical assessment plus available data from laboratory analyses on destructive samples). Contrary the other INSIDER datasets, no in situ measurements were available. However, a spatial regression model has been used to mimic the output of activation model computations.

After shutdown, the reactor G2 was sampled through channels, a horizontal core and a vertical core. Each sample (cores) or sampling location (channel) provide subsamples. In horizontal and vertical cores, each subsample was analysed one to three times, which permits dispersion analyses on the duplicates. A variability analysis is then performed at the different scales: the variability between samples is always higher than the variability of its constituting elements (subsamples and then duplicates). It means that the variability at the sample-scale is meaningfully lower than the variability in the graphite-scale, which justifies using spatial tool (in particular geostatistical variogram) in order to break the different variability contribution down and quantify them.

Then two evaluation objectives were pursued: global estimates of total activity (source term or radiological inventory) and local categorization of volumes according to a radiological threshold for waste acceptance. Several statistical and geostatistical approaches are compared to quantify the impact of model parameters such as dealing with measurement uncertainty and detection limits, integration of an auxiliary model in a multivariate approach... As full part of the INSIDER project, a specific focus is put on uncertainty quantification. Conclusions vary for the different nuclides as their physical behaviour in the reactor after activation can be significantly different, which significantly impact the statistical and spatial variability.

1 Annex 4: UC3b Summary

1.1 Overall strategy

1.1.1 Request for initial characterization

G2 is an UNGG reactor localized at the CEA center of Marcoule that was operated during 22 years until 1980 [1]. For D&D operations on this facility, the initial characterization focuses on the graphite volume presented on Figure 1. This is a horizontal prism of 9.53 meters by 9.40m, 9.05 meters long and with a radius of about 4.7 meters. The G2 graphite is composed of 1000 tons of moderator surrounded by 302 tons of reflector.

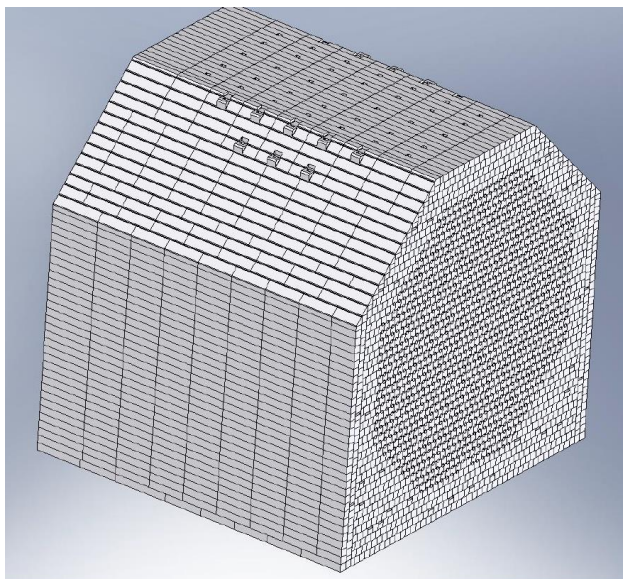


Figure 1 : General representation of the graphite volume from G2 reactor (Assystem EOS).

1.1.2 Define objectives

The main objective is to provide a radiological inventory for the graphite volume. Some key nuclides will be of key interest for specific nuclides in a waste repository perspective.

A secondary objective is waste oriented with the classification of volumes according to different thresholds.

Due to confidentiality reasons, real numerical values will be hidden throughout the rest of the document. Only relative quantification will be provided.

1.1.3 Gather pre-existing records/data

After shutdown, the reactor G2 was sampled through channels, a horizontal core and a vertical core (Table 1). The acquired samples through the cores and channels were analysed to investigate activity of the present radionuclides (Figure 2), as a consequence of activation or fission during the service of the G2 reactor.

Table 1. Acquired samples through graphite of G2 reactor, after shutdown [2].

Core name	Sampling date	Core length	Analysed radionuclides
W17 and W14P	April 1980	Punctual sample	C-14, Co-60, Ba-133, Cs-137, Eu-152+154, Eu-155
E15S, E18L, E21A, E27G, E32K, W11F, W07K, W25L and W28Q	April 1981	Data not available	Data not available
E11J, E17B, W28B, W17B, W11B, W14B, W7B, W1B, W4B and W20B	April 1984	Data not available	Data not available
Horizontal core	8-9 February 1988	13-20 cm	H-3, C-14, Cl-36, Ni-59, Ni-63, Cr-51, Mn-54, Co-57, Co-58, Fe-59, Co-60, Nb-94, Ba-133, Cs-134, Cs-137, Eu-154, Eu-155, Ho-166m, Am-241, Pu-239-240, Pu-238+Am-241, Cm-242, Cm-243-244
Vertical core	1989	20 cm	

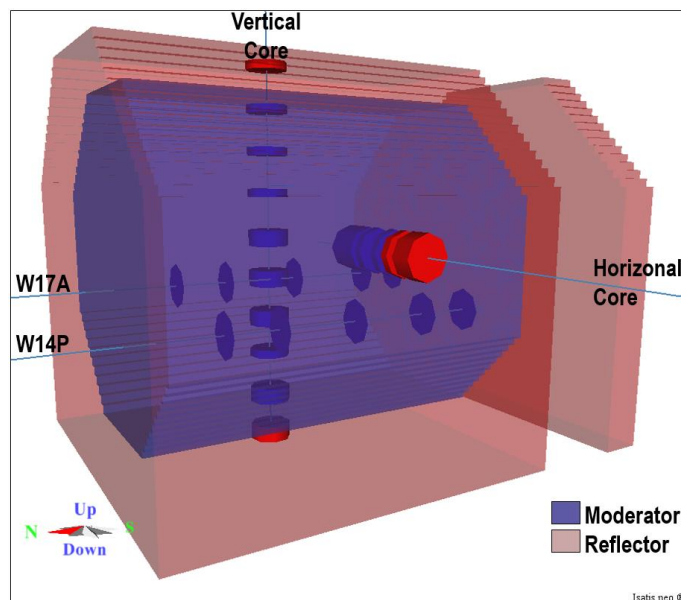


Figure 2. Location of graphite samples acquired from the moderator or reflector.

1.1.4 Is data sufficient for analysis? Can more samples be collected?

As there is no possibility for new samples and new in situ measurements, the existing dataset is considered as the final one within the INSIDER project for this use case 3b.

1.2 Data analysis & sampling design

1.2.1 Pre-processing

Each sample was divided to subsamples (Figure 3). In horizontal and vertical cores, each subsample was analysed one to three times, which permits dispersion analyses on the duplicates (Figure 3a and §1.2.2.1). However, in the channels, no duplicate analysis was performed, and the reported activity is the average of Type 1 (T1) and Type 2 (T2) analyses (Figure 3b), which are equivalent to the subsamples in the cores. Related dispersion is analysed in §1.2.2.2 for horizontal and vertical cores, on the one hand and in §1.2.2.3 for channel data on the other hand. In addition, the tritium (H-3) duplicates were analysed by two different methods A1 and B2, detailed in §1.2.2.2 along with other leaching (lixiviation in French language) results. In the next chapter, statistical analysis on the subsamples and duplicates is reported.

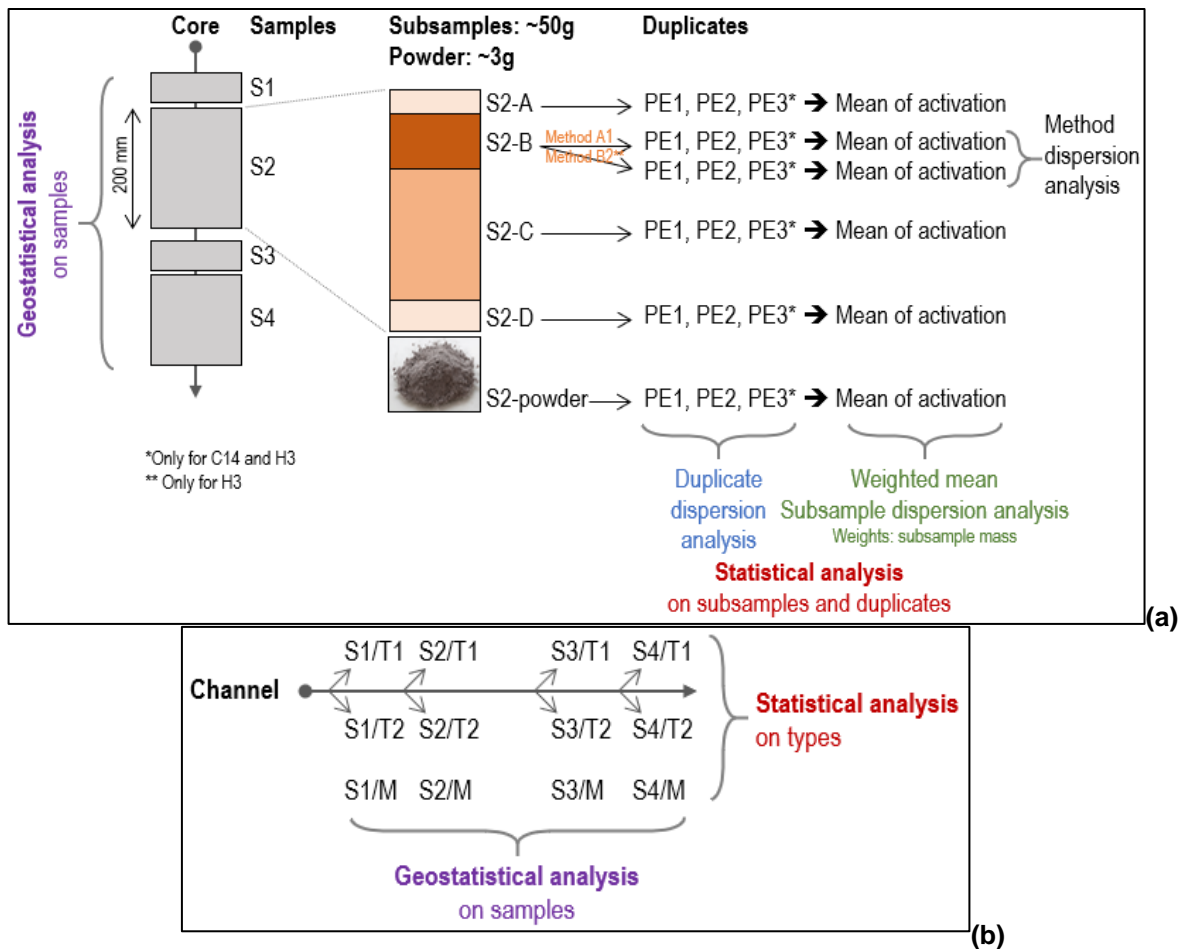


Figure 3. Sampling, subsampling and duplicate analyses in horizontal and vertical cores (a), also in channels (b).

Data excavation was done to match duplicates in the database of horizontal and vertical cores (Figure 4). During data excavation and primary exploratory data analysis, some incompatibilities were observed in the database:

- Radionuclide H-3, sample #1 of horizontal core (H1): mistake of subsample indices (H1-A and H1-B) was corrected according to other associated information: measurement date, subsample name and mass.
- Radionuclide H-3, subsamples H1-B, H1-C, H3-A, H5-A, H5-C, H7-p, H10-p and V27-7-Aini: Some duplicates (PE1, PE2 and PE3) or their averages were repeated by methods A1 and B2.
 - Radionuclide H-3 in sample H1 is removed because of high variability between activity of subsamples.
 - On five subsamples, both the Methods A1 and B2 were applied. Their results were very close but for subsample H3-A (Figure 11). In this subsample, Method A1 is preferred since Method B2 has an extreme value.
- Radionuclide C-14, subsample V22-D: the subsample name in the dataset contains an extra “G2”, compared to other subsample names.
- Two “non id” records for sample H12 (date 1988): radionuclides C-14 and Cl-36. They were ignored. In the same interval, sample H12-C (date 2016) contains information.

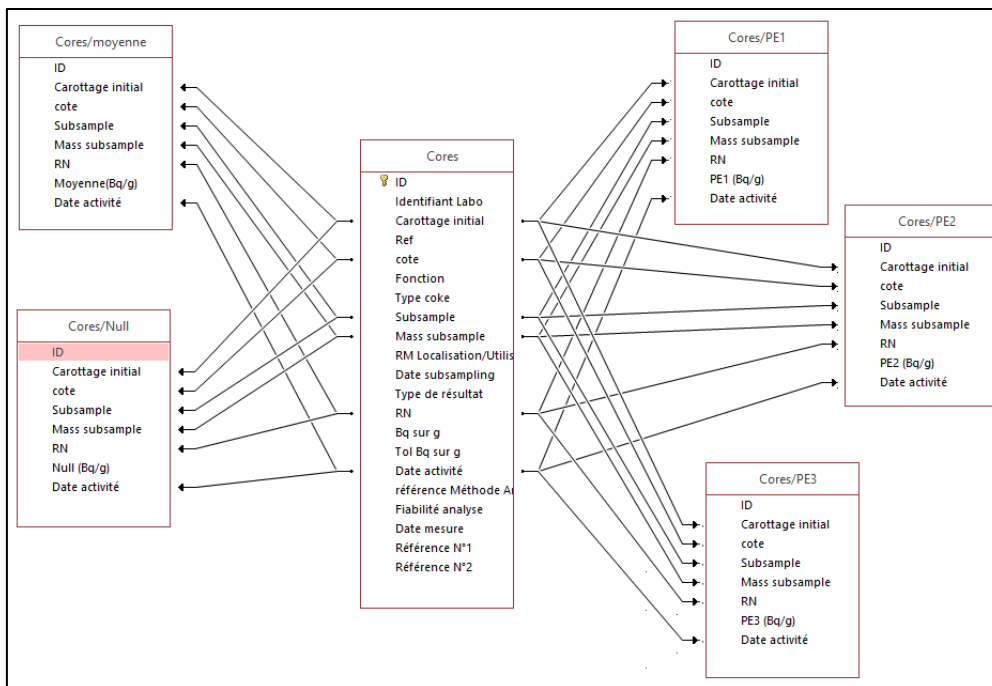


Figure 4. Searching duplicate activities of horizontal and vertical core, according to six characteristics: (i) core type, (ii) sampled interval in the core, (iii) subsample name, (iv) subsample mass, (v) radionuclide and (vi) activity date. Microsoft Access software is used.

1.2.2 Exploratory data analysis

1.2.2.1 Dispersion of measurement repetitions (duplicates)

To control the quality of data, average and standard deviation of duplicates activity measurements (PE1, PE2 and PE3) is calculated. The calculated average is compatible with the reported activity but in three subsamples (Figure 5a). Two of them are lower than the detection limit but for Eu-155, the reported average is false. In addition, some subsamples have duplicates, but the average is not reported. The calculated coefficient of variation is considered, and compared to the average value, which seems to decrease while activity concentration increases. (Figure 5b). Average of coefficient of variation of duplicates is calculated for duplicates of each radionuclide, which is always less than 15% (Figure 5c). The latter graph will be completed throughout the document with other coefficients of variation at larger scales for a proper and visual comparison.

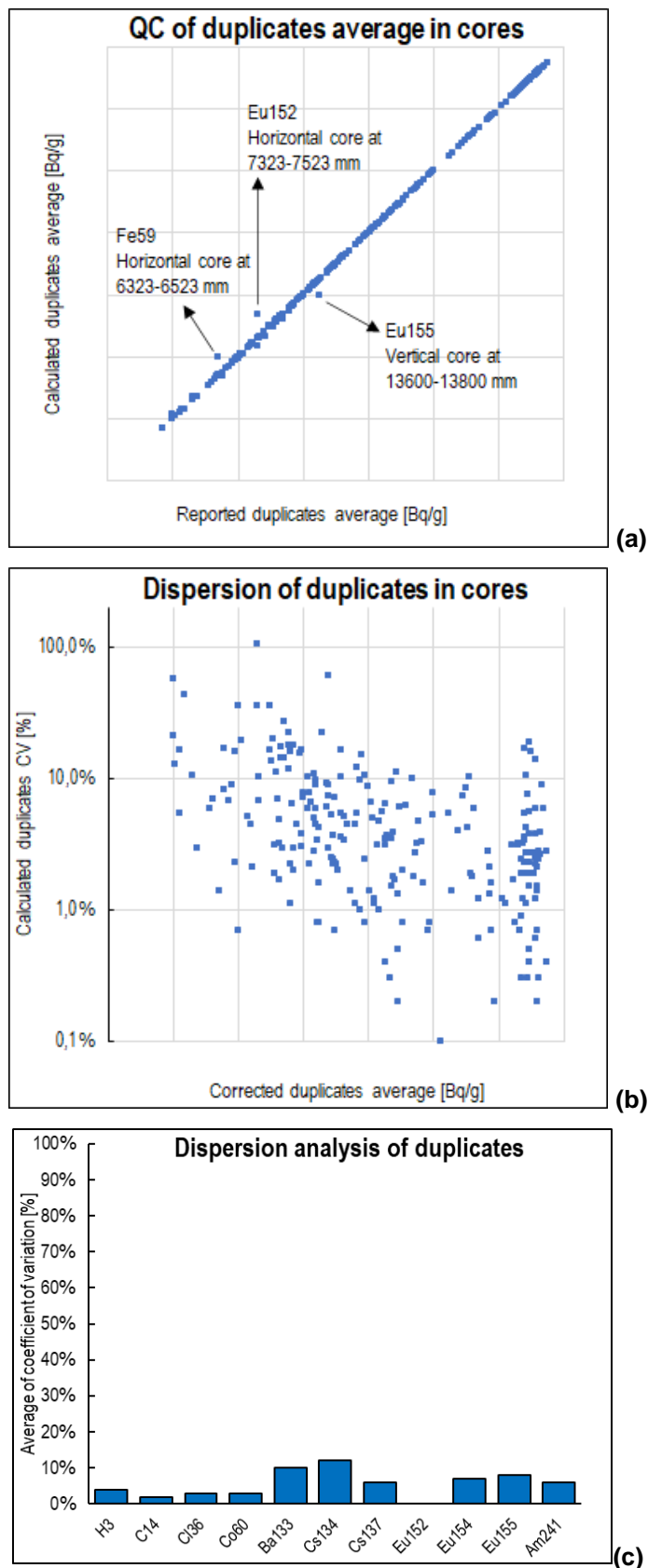


Figure 5. Comparing reported and calculated log₁₀ average of duplicates (a). Coefficient of variation of duplicates versus the log₁₀ average (b). Average of coefficient of variation in each radionuclide (c).

1.2.2.2 Dispersion within core subsamples

The core subsamples were averaged (weighted to the mass) to calculate the activity of samples. Also, weighted standard deviation was calculated and plotted against the weighted average (Figure 6a). The standard deviation is reasonably low compared to the activity values. For the lower activities, standard deviation fluctuates more, which is due to imprecision of low values. Average of coefficient of variation of duplicates is calculated for subsamples of each radionuclide, which is always less than 45% (Figure 6b).

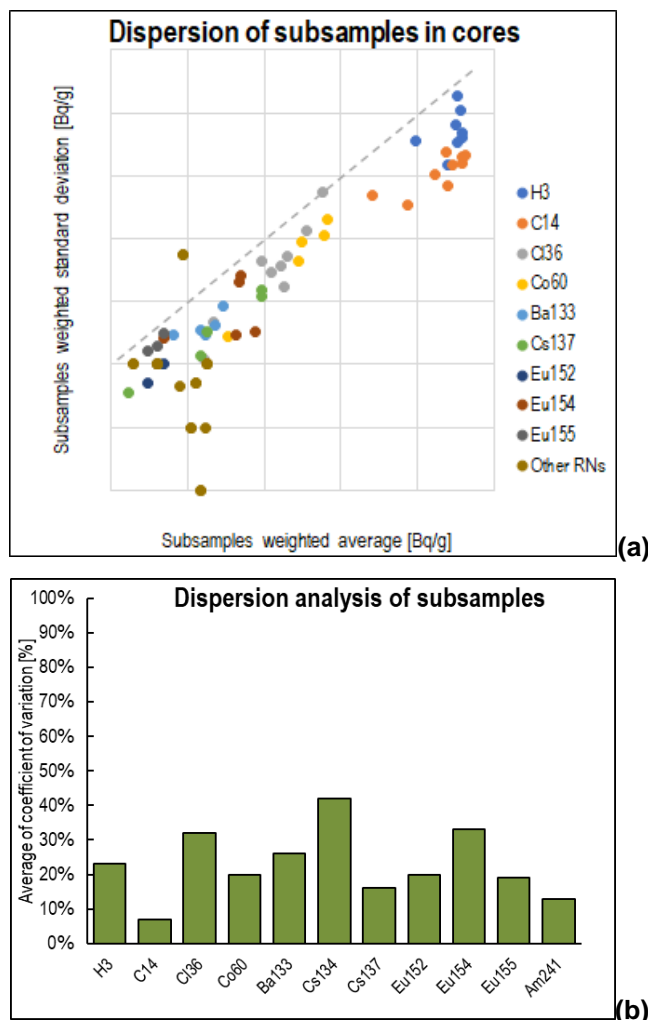


Figure 6. Comparing the weighted log₁₀ average of subsamples and their log₁₀ standard deviation (a). Average of coefficient of variation in each radionuclide (b).

1.2.2.3 Dispersion of channel types

Data excavation was done to match the corresponding types within the channels database (Figure 7). During data excavation, some incompatibilities were observed in the database (Figure 8a):

- Decimal error in duplicates: Cs-137 and Eu-155 (W14P)
- Reported average was incorrect (a systematic computation problem when only one duplicate exists):
 - Ba-133 (W17A twice)
 - Cs-137 (W14P and W17A)
 - Eu-155 (Vertical core at R1 subsample, W14P and W17A)
 - Eu-152+154 (W14P and W17A)

The corrected activity average was compared to the standard deviation of type pairs (Figure 8b). The standard deviation is reasonably low compared to the activity values, which confirms the

precision of the available dataset of channels. Average of coefficient of variation of duplicates is calculated for types of each radionuclide, which is always less than 20% (Figure 8c).

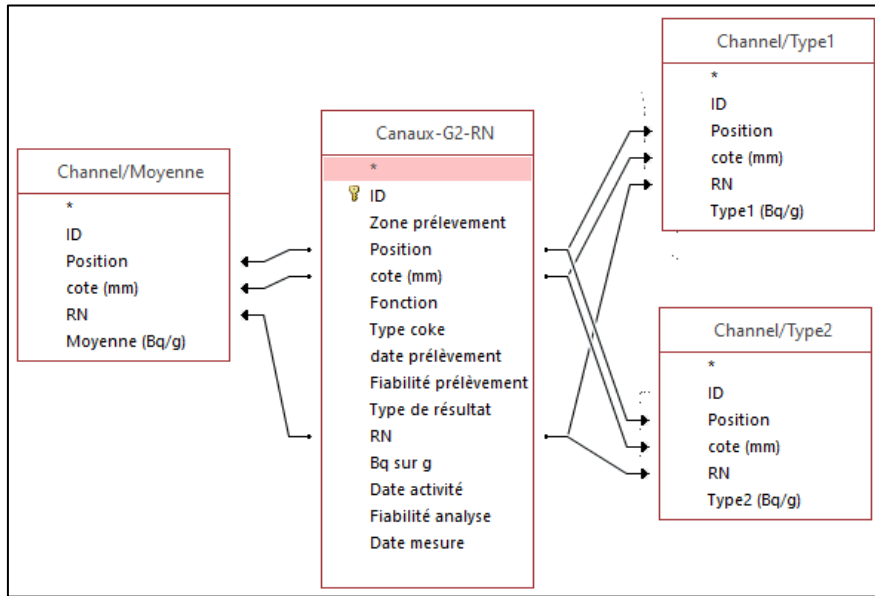


Figure 7. Searching types in channels, according to three characteristics: (i) channel position, (ii) sampled interval in the channel and (iii) radionuclide. Microsoft Access software is used.

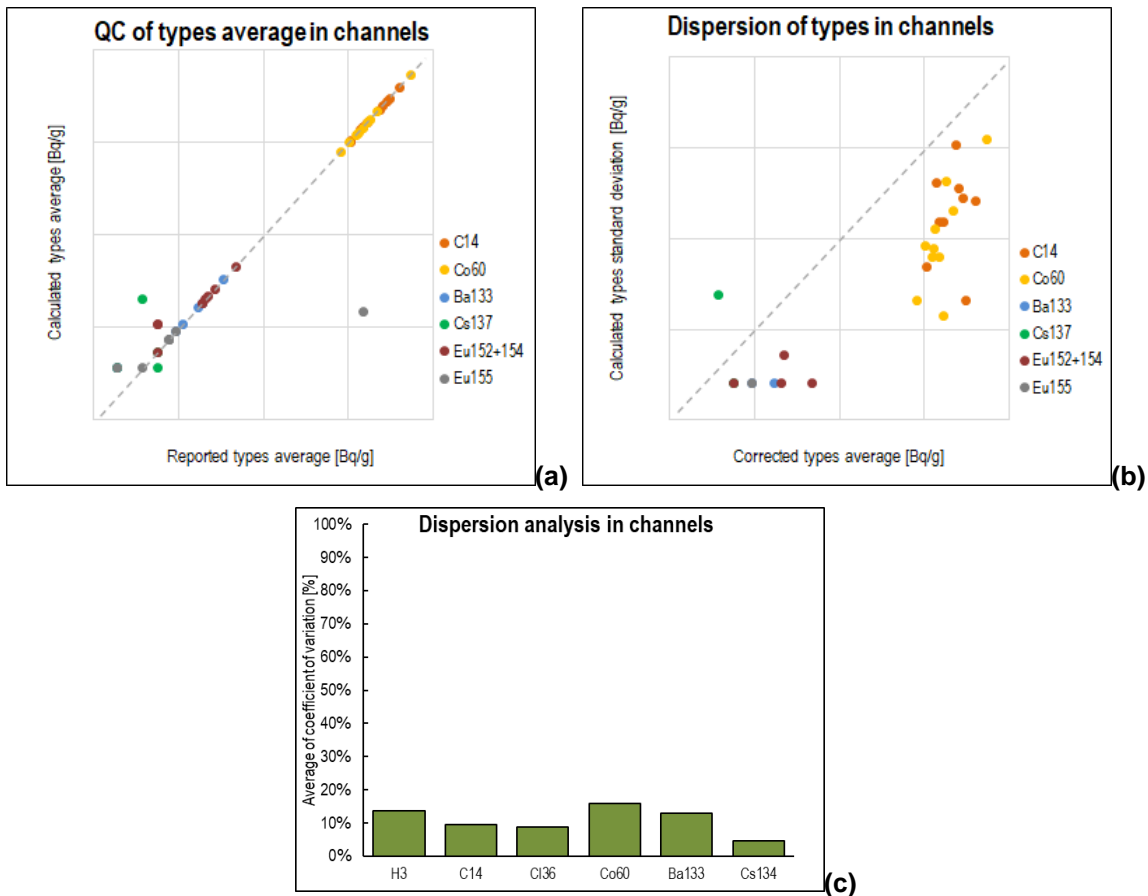


Figure 8. Comparing the reported and calculated log10 average of type pairs activity (a). Comparing the weighted log10 average of type pairs and their log10 standard deviation (b). Average of coefficient of variation in each radionuclide (c).

1.2.2.4 Comparing analysis protocols

The activity measurement (analysis) were done by either of three protocols:

- **LARC MA:** Conforming with Figure 3, each sample was divided into subsamples with known subsample mass:
 - In horizontal and vertical cores: Measurement date is between 9/15/2008 and 7/9/2018. Available duplicates PE1 and PE2 (Figure 3a) were compared (§1.2.2.1).
 - In channels: Measurement date is 23/5/1980. The available average value (type 1 and type 2, Figure 3b) were compared (§1.2.2.3).
- **SPR Marcoule 1989:** No subsampling and the sample mass is not reported. The measurement date is 14/12/1989 (SPR Marcoule). Only applied to some samples in the vertical core.
- **Leaching 2004:** The analyses related to leaching (lixiviation in French language) process. The measurement date is 9/3/2004. Only applied to one sample in the vertical core (V36).

The three protocols could be compared in the vertical core (Figure 9). At the horizon 9.5 m, LARC MA and SPR Marcoule 1989 protocols were applied to the same sample, and between the horizons 12 m and 18 m, LARC MA and SPR Marcoule 1989 protocols could be compared by five adjacent sample pairs with distance of 20 cm. At the horizon 15.4 m, SPR Marcoule 1989 and leaching 2004 protocols were applied to the same sample.

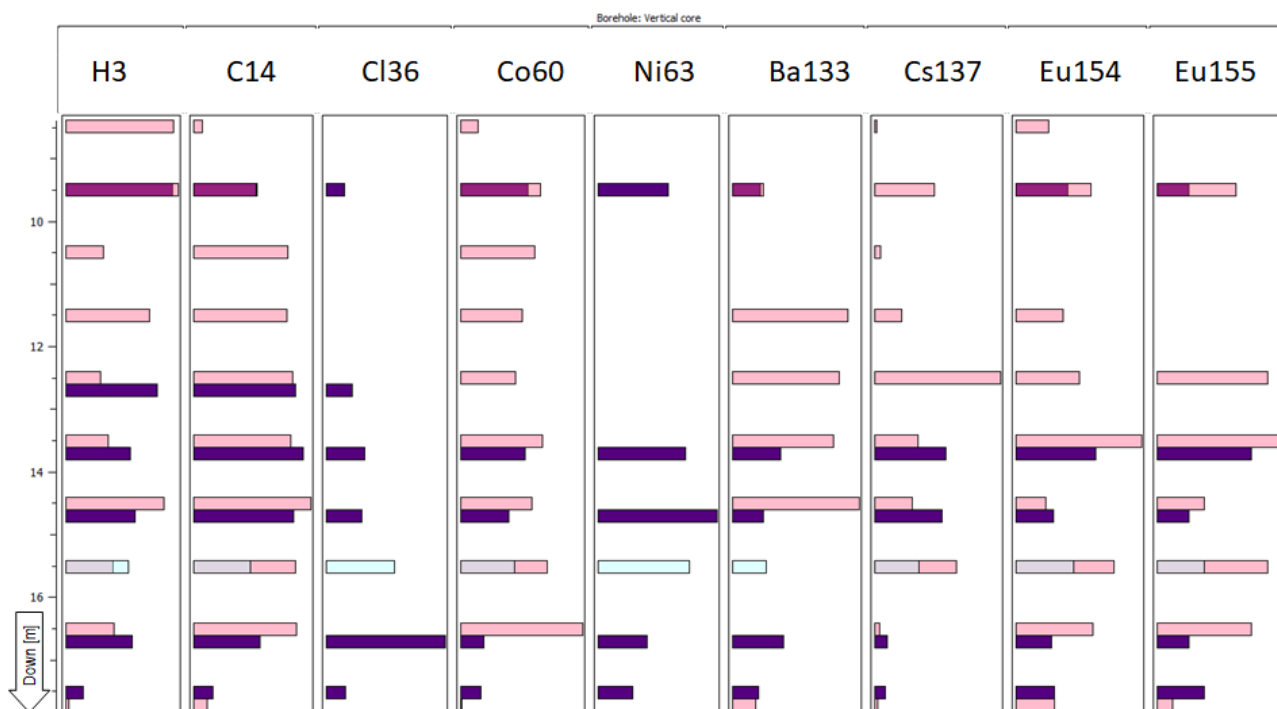


Figure 9. Profile of activity of radionuclides in the vertical core of the G2 reactor graphite, according to the analysis protocol: SPR Marcoule 1989 in purple, LARC MA in pink, Leaching 2004 in blue.

The protocols results are highly correlated (Figure 10). The activity of SPR Marcoule 1989 protocol is systematically higher than the activity of LARC MA protocol but for tritium and Cs-137 (Figure 10a), which is not related to the radioactivity decay (all corrected to 1/1/2016). Despite the general compatibility of the analysis protocols, there are some unjustified incompatibilities on the vertical core (Figure 10a), e.g.: H-3 (at 12.5 m), Co-60 (at 16.5 m), Ba-133 (at 13.5 m and 14.5 m), Cs-137 (at 13.5 m, 14.5 m, 16.5 m and 17.5 m), Eu-154 (at 13.5 m and 16.5 m) and Eu-155 (at 11.5 m, 13.5 m, 16.5 M and 17.5 m). In addition, coefficient of variation of the LARC MA measurement versus the SPR Marcoule 1989 one (proportionally higher globally) is presented on Figure 10c. The coefficients of variation are comparable since calculated on the same number of data (samples with the distance of maximum 20 cm).

In order to have more homogenous and uniform dataset, the data SPR Marcoule 1989 and Leaching 2004 were exempted from further analyses. So, statistical and geostatistical analysis are limited to the activity measured by the LARC MA protocol.

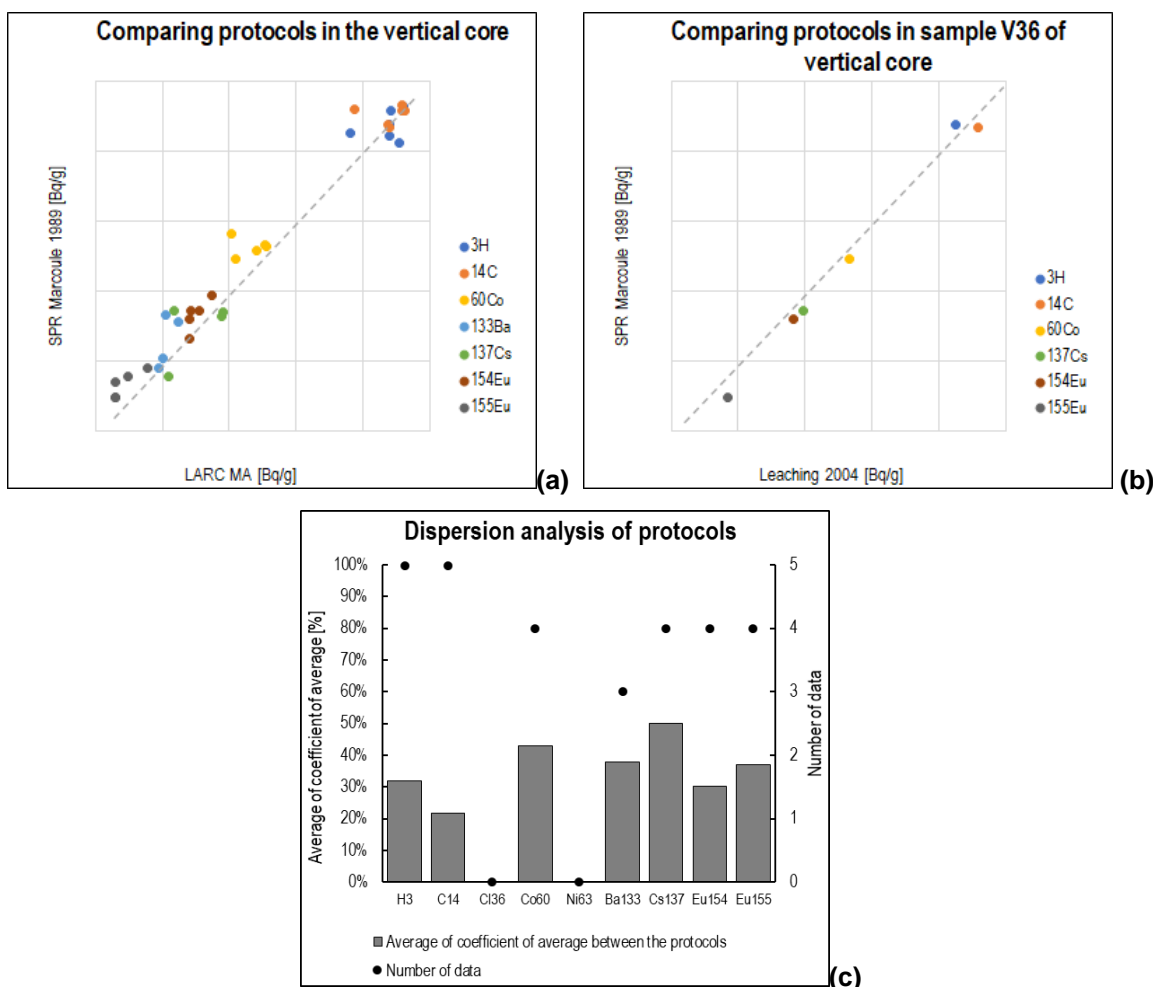


Figure 10. Comparing log10 measured activity by protocols LARC MA and SPR Marcoule 1989 for the samples with the maximum distance of 20 cm (a). Comparing the log10 measured activity by protocols leaching 2004 and SPR Marcoule 1980 for the sample V36 at 15.4 m on the vertical core (b). Comparing coefficient of variation of measurement protocols for of each radionuclide (c).

1.2.2.5 Comparing analysis methods for Tritium

In five subsamples, tritium (H-3) duplicates were analysed twice by LARC MA protocol: methods A1 and B2. The results are very similar in four subsamples but not similar in H3-A (Figure 11a). In addition, the calculated average confirms the quality of reported average (Figure 11b). In subsample H3-A, method A1 is preferred since method B2 results in higher values, far from other subsamples.

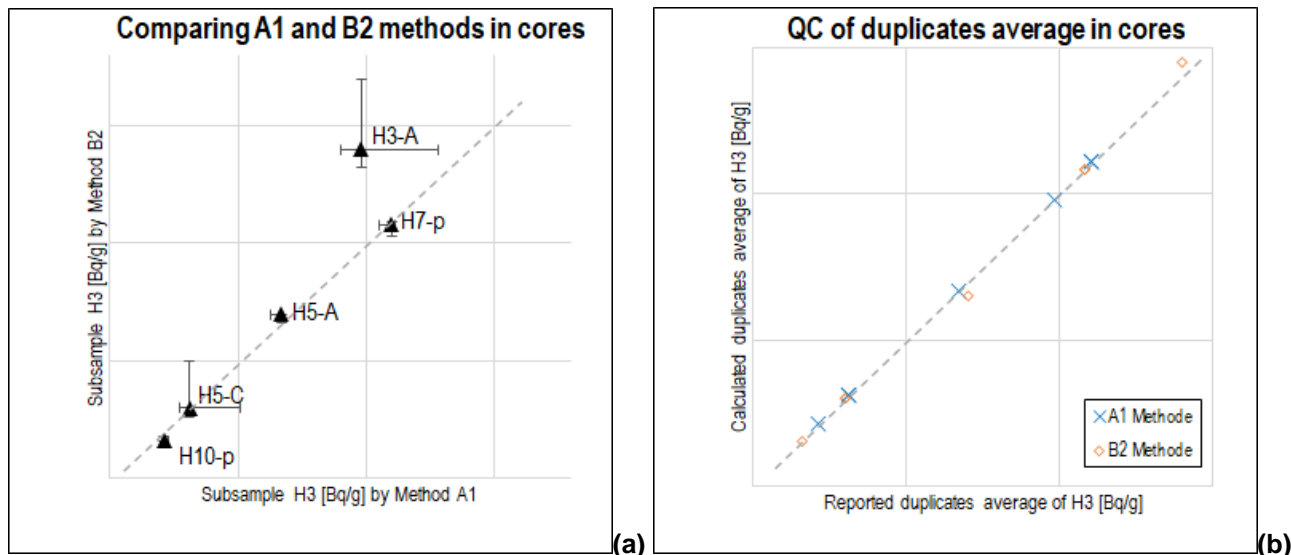


Figure 11. Comparing reported average of tritium (H-3) activity by two methods A1 and B2 (a). Comparing reported and calculated average of duplicates of H-3 (b).

1.2.2.6 Synthesis of dispersion analyses

Two sources of data (cores and channels) were excavated to extract:

- From cores:
 - Core duplicates
 - Core subsamples (average of core duplicates)
 - Core samples (weighted average of core subsamples)
- From channels:
 - Channel types
 - Channel samples (average of channel types)

Conforming to Figure 3, statistical and dispersion analyses were applied to these multiple datasets in order to perform a quality control, also to prepare a reliable dataset for further geostatistical analyses (§1.2.4). Dispersion analysis was done using the average of coefficient of variation on duplicates, subsamples and types (Figure 12).

Core duplicates is the most homogeneous dataset. Core subsamples is the most heterogeneous dataset, in general. The exceptions are C-14 where channel types are more heterogeneous and Cs-137 where channel types and core subsamples have the same heterogeneity.

Homogeneity of core duplicates confirm the reliability of laboratory analyses. Core subsamples are heterogeneous in some radionuclides, which will result in uncertain core samples for the geostatistical analyses. In addition, relatively homogeneous channel types assure the channels samples for the geostatistical analyses.

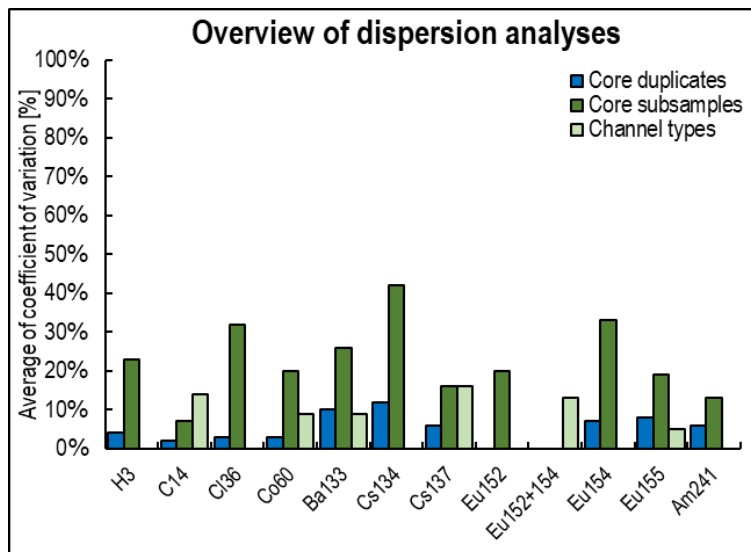


Figure 12. Comparing dispersions between core duplicates, between core subsamples and between channel types.

1.2.3 Data analysis with statistical tools

After discussion with experts from CEA and considering the operational background of the facility, the existence of an axial symmetry for the activities was considered as a relevant hypothesis. Furthermore, activation calculation have been performed by CEA to have an estimation of activities in the graphite. Activity measurement data obtained are very few but associated with localization information as radial coordinate. Considering the context of this characterization problem, geostatistical approach provides estimation with a large prediction error due to the small data sample on a very restricted distribution area, moreover, simulations with such a geostatistical model outside the convex hull of the data will be in this case extrapolation with little confidence. Therefore, we have used the CARTOSTAT methodology (FRANCE Patent No. 1906548, 2019) to develop a probabilistic model to provide realistic activity estimations. An Excel file containing all measurement data and uncertainty measurements associated to localization information elaborated by the CEA LARC laboratory has been communicated to us. Table 2 presents the number of available measurement data and variation range of measurement uncertainties for the 13 studied radionuclides. For all data, we have also an information for the localization but considering the size of data set for each radionuclide, only ^{14}C , ^{36}Cl et ^3H have been treated by the spatial statistical method CARTOSTAT1 and for the others we have used CARTOSTAT0D without taking into account the spatial. The activity estimations have been calculated for the whole volume of graphite considering a density of 1.7.

RN	Data set size (+outliers)	Uncertainty range
¹⁴ C	55	[5% ; 27%]
³⁶ Cl	47(49)	[11% ; 35%]
³ H	49(52)	[1% ; 43%]
¹³³ Ba	18	[7% ; 120%]
¹³⁷ Cs	17	[8% ; 90%]
¹⁵⁴ Eu	18	[8% ; 43%]
¹⁵⁵ Eu	11	[22% ; 149%]
²³⁸ Pu+ ²⁴¹ Am	15	[2% ; 54%]
²³⁹ Pu+ ²⁴⁰ Pu	14	[1% ; 40%]
²⁴³ Cm+ ²⁴⁴ Cm	11	[9% ; 200%]
⁵⁹ Ni	14	[16% ; 70%]
⁶⁰ Co	18	[5% ; 23%]
⁶³ Ni	17	[8% ; 26%]

Table 2: Number of available data and variation range of measurement uncertainties for the 13 studied radionuclides.

The CARTOSTAT methodology performs a statistical approach taking into account uncertainty measurements and limits of detection with a specific treatment considering these data as incomplete information.

For ³⁶Cl radionuclide, 49 data measurement data with uncertainties are available with 2 outliers qualified as not reliable by CEA experts as we can see on Figure 13 (a). These two data have been rejected. Figure 13 (b) show data dispersion according to radial coordinates. The histogram of measurement data on Figure 14 (a) shows an asymmetric distribution close to a lognormal distribution. The dispersion of measurement uncertainty presented on Figure 14 (b) is asymmetric between 11 and 35%.

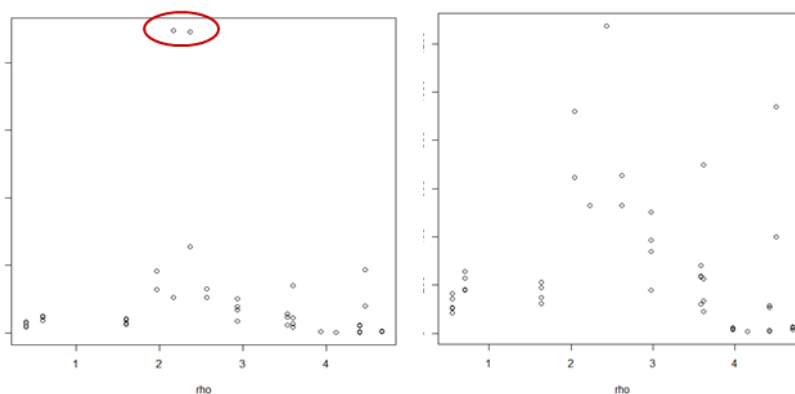


Figure 13 : Dispersion of measurement data for ³⁶Cl according radial coordinate with two identified outliers on left (a) and without outliers on right (b).

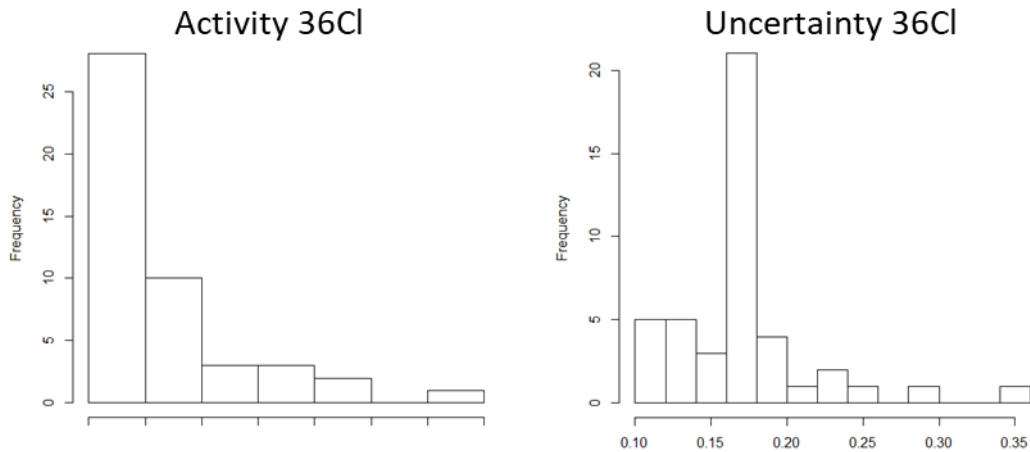


Figure 14: Histograms for ^{36}Cl activities on left (a) and for relative uncertainty measurements on right (b).

For confidentiality reasons, numerical results are not presented. Table 3 presents relative differences on total activity of ^{36}Cl estimated by statistical activity estimations of ^{36}Cl for mean, median and high quantiles provided by models without and with uncertainty treatment. The model with uncertainties treatment gives estimations significantly lower than those of model without uncertainty treatment for all the statistical indicators: mean, median and high quantiles provided. As we can see on Figure 15 compared to valid data, performances of both models are similar for median and 90%-quantile (51% of the points over the median curve and 10.6% of points over 90%-quantile curve). Nevertheless, for 95-quantile there is an small overestimation for the model without uncertainty treatment and a small underestimation for the model with uncertainty treatment (4.25% of points over the 95%-quantile curve for the model without uncertainties and 6% of points over the 95%-quantile curve for the model with uncertainties).

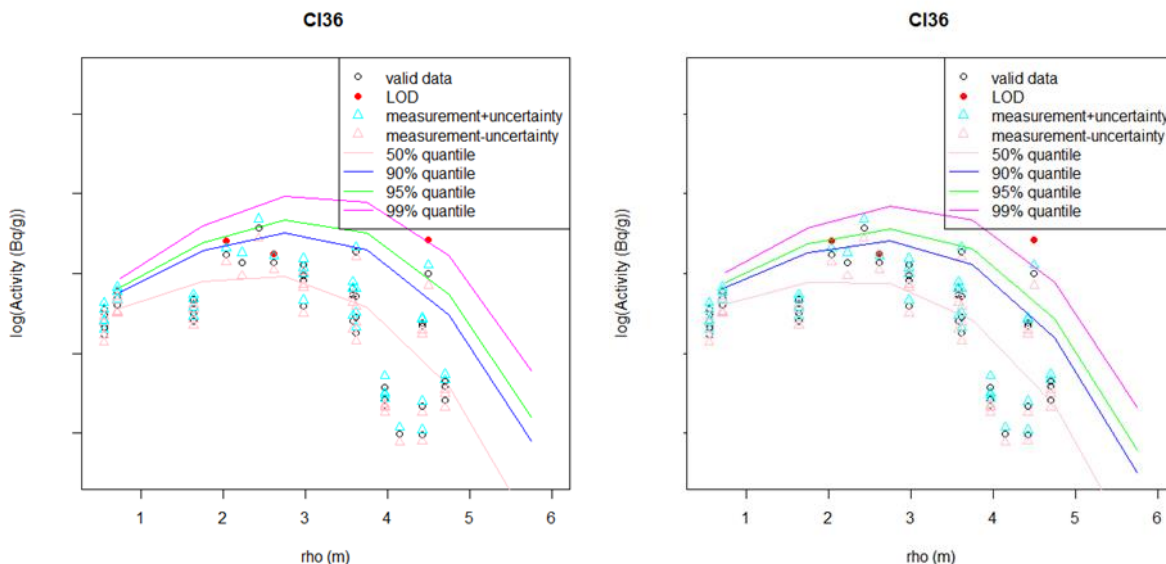


Figure 15: Activity and uncertainty measurements for ^{36}Cl according to axe distance and quantile curves for statistical models without uncertainty treatment on left (a) and with uncertainty treatment on right (b).

^{36}Cl	Difference without and with uncertainties
median	15.79%
mean	23.33%
quantile _{90%}	25.00%
quantile _{95%}	16.05%

Table 3: Difference on total activity of ^{36}Cl estimated by statistical models without uncertainty treatment and with uncertainty treatment.

Figure 16 gives a cartography of ^{36}Cl activity radial repartition in the graphite for median and 90%-quantile estimations provided by the model with uncertainty treatment.

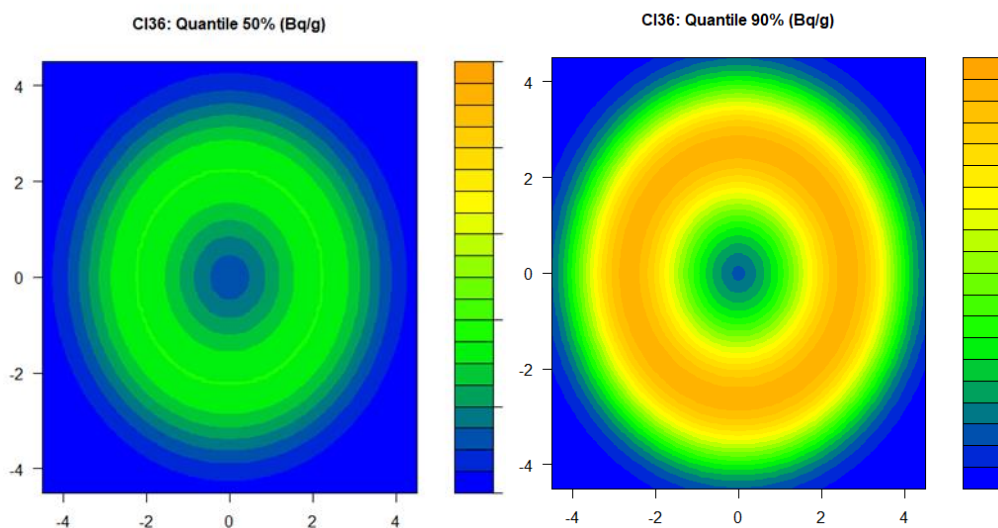


Figure 16: Graphical representation of activity repartition of ^{36}Cl estimated by the statistical model with uncertainty treatment with median on left (a) and 90%-quantile on right (b).

Figure 17 shows lognormal fitting obtained for non-spatial data of ^{133}Ba without uncertainty treatment (a) and with uncertainty treatment (b). Graphical results are in favour of the model with uncertainty treatment, which has been confirmed by statistical tests.

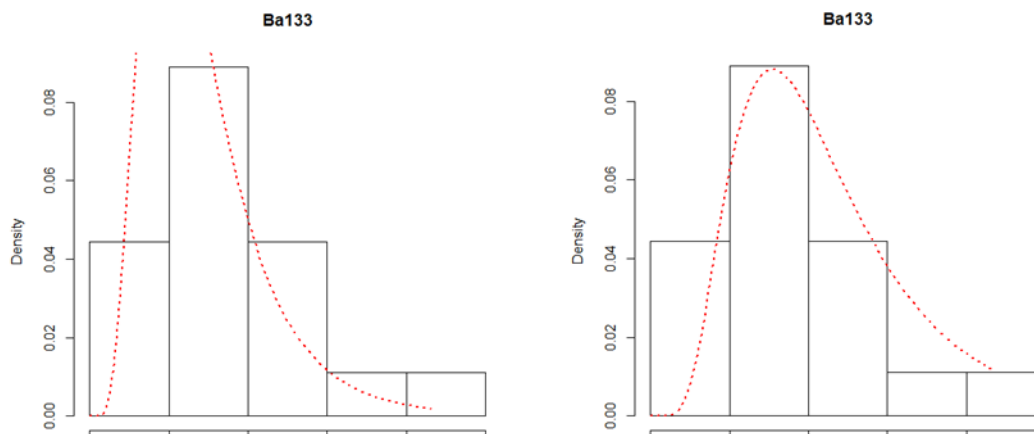


Figure 17 : Lognormal distribution law fitted without uncertainty treatment on left (a) and with uncertainty treatment on right (b) for activity measurement data of ^{133}Ba .

For the measured radionuclides in the graphite drillings of G2 reactor, all the 95% confidence intervals provided by CARTOSTAT with uncertainty treatment are very close to 95% confidence intervals produced by activation simulations. As we can see on Figure 18, for 9 radionuclides the confidence intervals estimated by CARTOSTAT methodology intersect confidence intervals estimated by activation simulations. For ^{36}Cl , ^{137}Cs and ^{63}Ni , CARTOSTAT estimations are more or less higher and for $^{243}\text{Cm}+^{244}\text{Cm}$, CARTOSTAT estimation is slightly lower than simulation forecasts. In this last case, the measurement data set is of size 11 with a large range of uncertainties, [9% ; 200%].

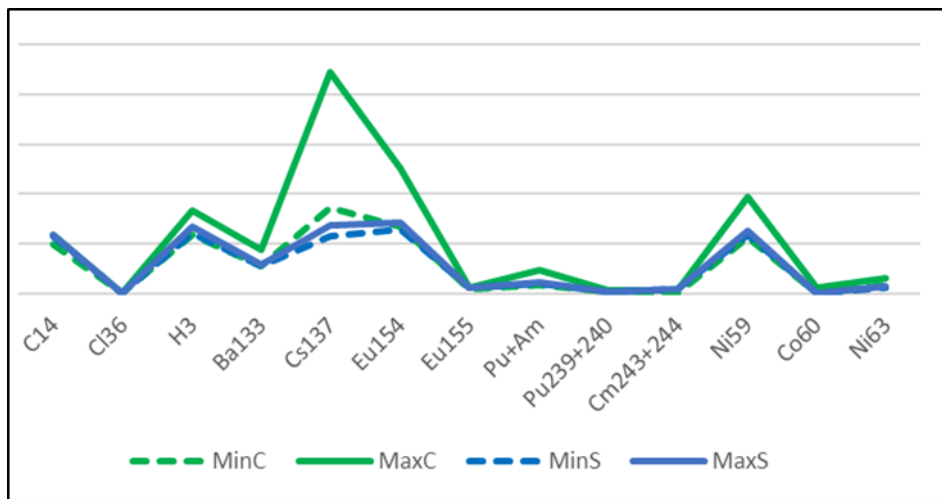


Figure 18 : 95% confidence intervals estimated by CARTOSTAT methodology and by activation simulations.

On Figure 19, we can see the representation of relative differences for total activity median estimations provided by models without and with uncertainties treatment with CARTOSTAT methodology. For four radionuclides ^{133}Ba , ^{60}Co , ^{154}Eu and $^{239}\text{Pu}+^{240}\text{Pu}$, estimations without uncertainty treatment are up to 95% less than estimations with uncertainty treatment. For four radionuclides ^{14}C , ^{36}Cl , ^{155}Eu and ^{63}Ni , estimations with uncertainty treatment are up to 28% less than estimations without uncertainty treatment. We do not give here all results from activation simulations but not to take account of measurement uncertainties provides confidence intervals that can be very different from simulation forecasts. These outcomes show the importance of measurement uncertainties treatment to provide realistic activity estimations.

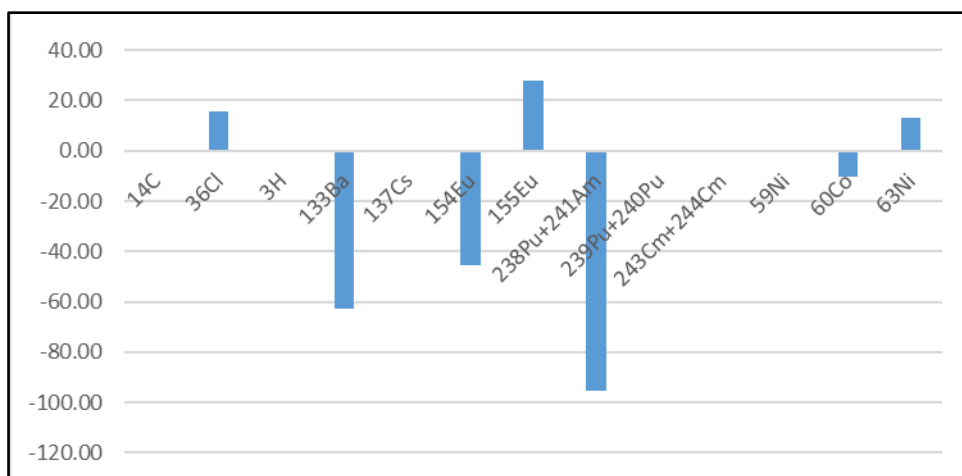


Figure 19 : Relative differences between median estimations without and with uncertainty treatment.

1.2.4 Data analysis with geostatistical tools

1.2.4.1 Statistical analysis of samples

The samples activity average of nine radionuclides were imported to the Isatis.neo (v.2020) software for geostatistical analyses. The activity date of all the imported radionuclides was corrected to 1/1/2016. It should be mentioned that the radionuclides with a few measurements higher than the detection limit were not imported, e.g. Eu-152 is always below the detection limit but in the first sample of the horizontal core from the reflector. Ni-59 is also exempted since the activity is very low, also not reported in the channels. Table 4 summarizes the number of imported samples which were used in spatial analyses.

Table 4. Number of imported samples, separated by radionuclide and core name.

Radionuclide	Product	Vertical Core	Horizontal core (Az=76.15°)	Channel (Az=166.15°)
3H	Activation	6	6	NO sample
14C	Activation	6	6	W14P: 5 W17A: 5
36Cl	Activation	6	7	NO sample
60Co	Activation	5	6	W14P: 5 W17A: 5
63Ni	Activation	5	7	NO sample
133Ba	Fission	5	7	W14P: 5 W17A: 2
137Cs	Fission	4	8	W14P: 2 W17A: 2
154Eu	Activation	5	7	NO sample
155Eu	Activation	5	6	W14P: 4 W17A: 3

Having too limited number of samples, they do not represent the whole graphite reactor. So, statistical analysis cannot be generalized to the whole graphite, especially in the reflector. The histograms of the activity of radionuclides are almost dissymmetric with low values in the reflector (Figure 20).

The cross-plots between the radionuclides show correlation in C-14 versus Co-60 and C-14 versus Cs-137 (Figure 21).

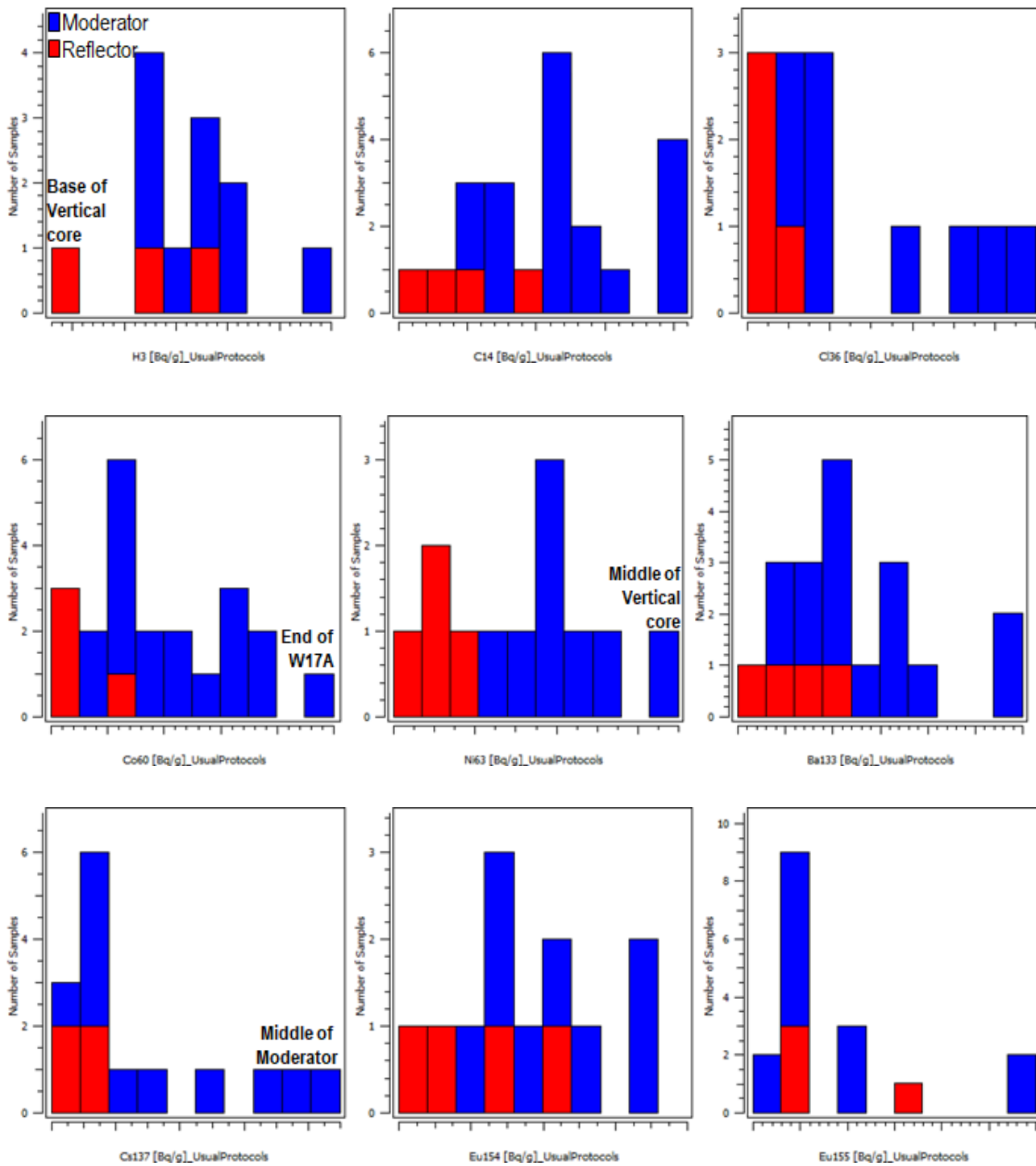


Figure 20. Histograms of the nine radionuclides in the graphite of G2 reactor.

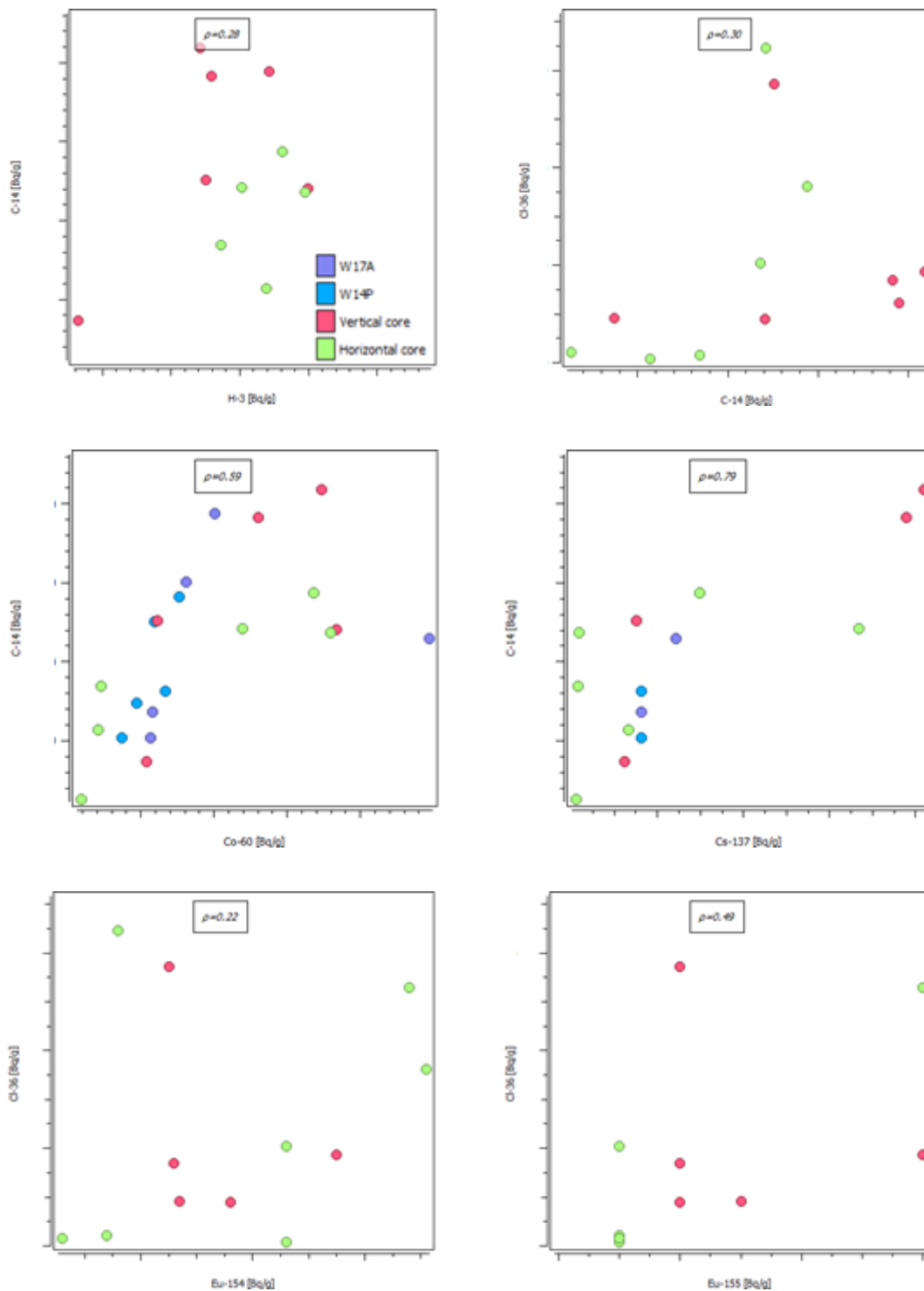


Figure 21. Cross-plots of activity of radionuclide C-14 versus H-3, Cl-36, Co-60 and Cs-137. Besides, Cl-36 versus Eu-154 and Eu-155 in the graphite of G2 reactor.

Coefficient of variation of samples is always higher than average of coefficient of variation of its constituting elements (duplicates, subsamples and types, as summarizes in Figure 12). It means that the variability in the sample-scale is meaningfully lower than the variability in the graphite-scale, which justifies using geostatistical tools (especially variography analysis) in order to analyse the spatial continuity between samples.

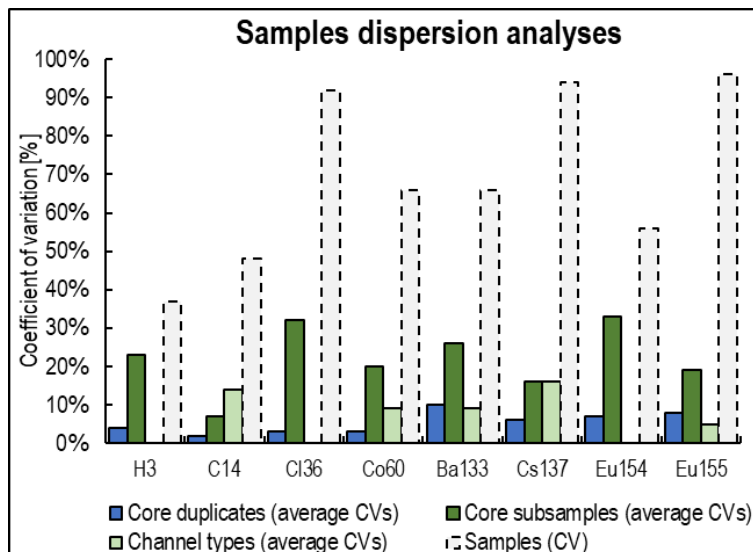
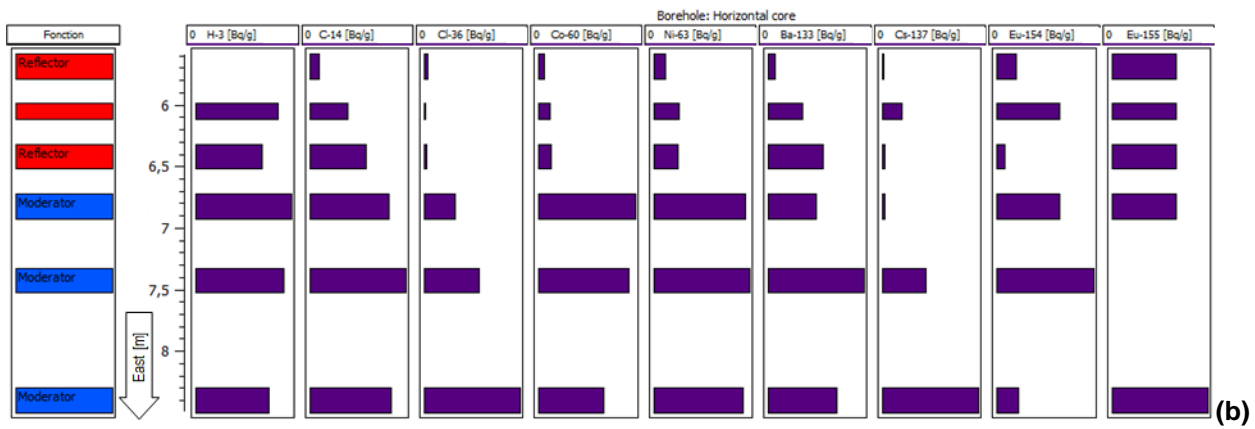


Figure 22. Comparing coefficient of variation (CV) of samples (global) with average of coefficient of variation of subsamples, duplicates and types.

1.2.4.2 Radionuclide profiles in graphite

The profiles of activity of the radionuclides were studied, and the observations are listed:

- Vertical core (Figure 23a):
 - The maximum activity is usually in the middle of moderator (horizon 13.5 m). H-3 and Cl-36 are the exceptions.
 - The minimum activity is usually in the bottom (reflector sample). For Cl-36, Ba-133, Eu-154 and Eu-155, the activity of reflector sample is minimal.
- Horizontal core (Figure 23b):
 - In general, activity rises eastward (toward centre of the reactor).
 - Reflector samples show meaningfully less activity than moderator samples.
- Channel W14P (Figure 23c): C-14, Co-60 and Ba-133 are maximum in the middle of the graphite.
- Channel W17A (Figure 23d): In general, C-14 and Co-60 increase southward, i.e. toward discharging face.



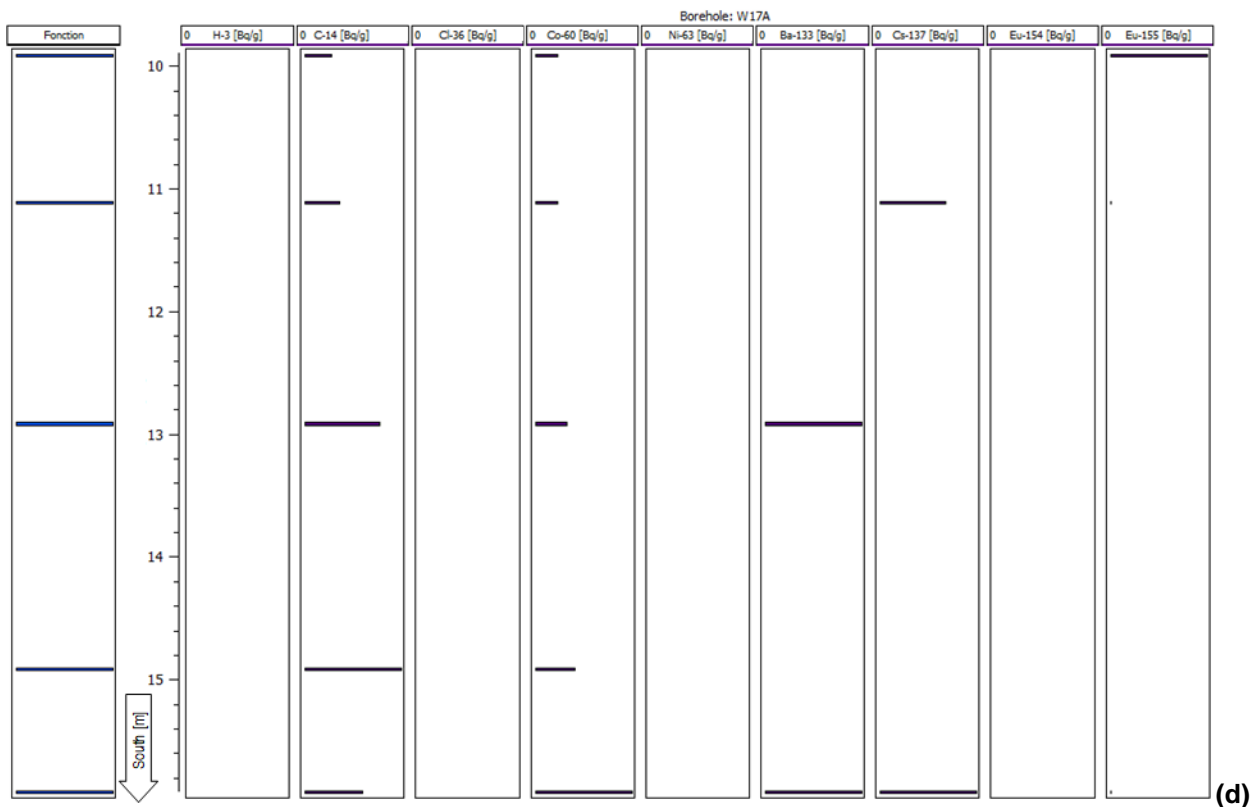
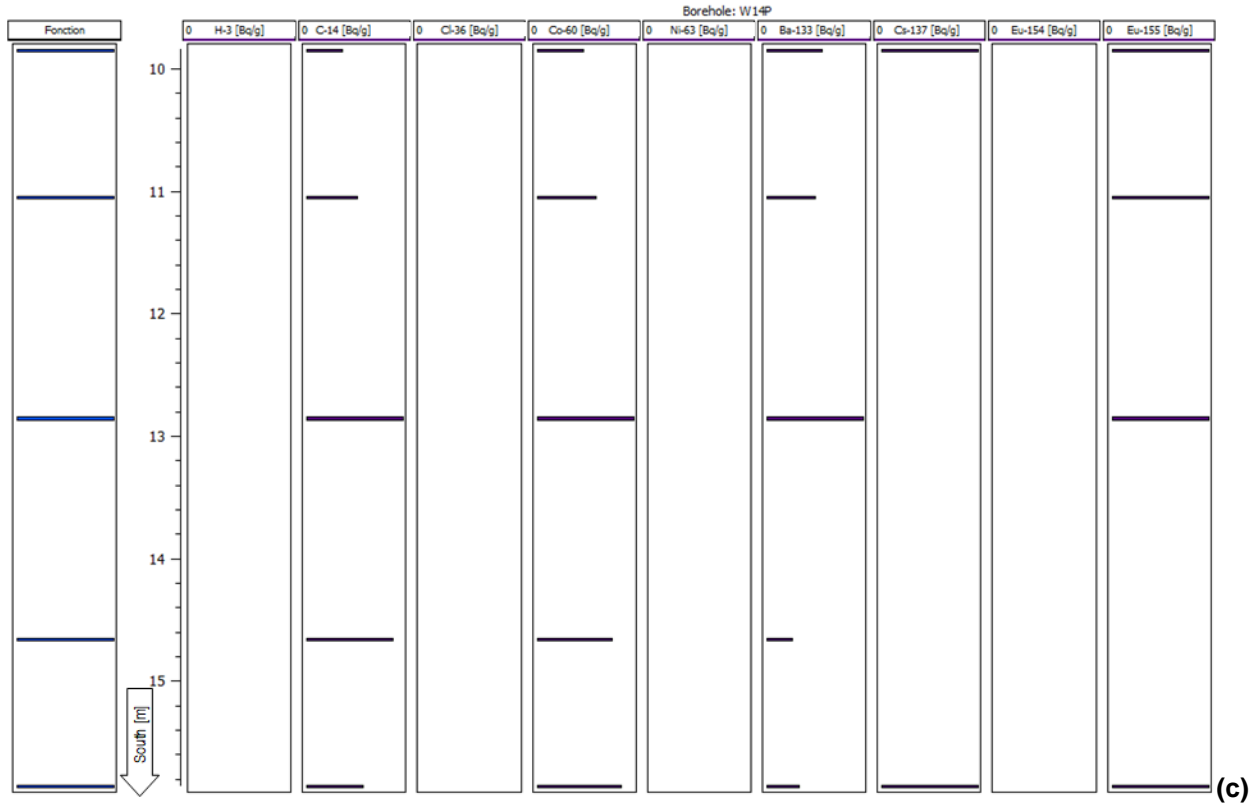


Figure 23. Profiles of activity of radionuclides (LARC MA protocol) in the G2 reactor graphite: vertical core (a), horizontal core (b), channels W14P (c) and W17A (d)

1.2.4.3 Variographic analysis of samples

The available samples were acquired along the drilling cores or channels. So, directional variography analysis was done to study spatial variability of radionuclides in each of three directions (Figure 24). A common observation among the different radionuclides is the limited nugget effect, i.e. negligible variability at zero distance. That is a spatial consequence of the relative proportion coefficient of variation of duplicate and subsample from the dispersion analysis (Figure 22) in comparison to the global statistical variability. However on the variogram, this variability is presented as a variance (the variability sill can be directly compared to the statistical variance reported on the histograms (Figure 20) instead of a coefficient of variation, which increases ever more the contrasts between the different variability contribution. For the specific observations on the spatial correlation, here they are listed:

- H-3: Vertical variogram reveals a trend, which is compatible with downward decrease of H-3 activity in Figure 23a. Horizontal variogram increases quicker, which might be due to location of horizontal core, which is at a high-variability zone (border of moderator-reflector). So, variability could be isotropic along vertical and horizontal directions.
- C-14: The variograms are conformable the most, due to available number of sample pairs. The spatial continuity is maximum parallel to the channels (lower variability). Spatial variability along vertical and horizontal cores have the same behaviour.
- Cl-36: In the vertical direction, variability is unchanged, while rises rapidly along the horizontal core. Horizontal variogram reveals a trend, which is compatible with eastward increase of Cl-36 activity in Figure 23b.
- Co-60: Along vertical core and channels, spatial variability has the same behaviour. Vertical variogram reveals a trend, which is compatible with downward decrease of Co-60 activity in Figure 23a. Horizontal variogram increases quicker, which might be due to location of horizontal core, i.e. at a high-variability border zone of moderator-reflector. So, variability could be isotropic along channels, vertical and horizontal directions.
- Ni-63: Activity variability is isotropic along vertical and horizontal cores.
- Ba-133: Horizontal variogram shows a spatial structure with high variability, and values much higher than variance (black dash-line). Vertical and channel variograms do not show spatial continuity (not enough data).
- Cs-137: Vertical variogram reveals a trend, which is compatible with downward decrease of Cs-137 activity in Figure 23a. Isotropic behaviour along vertical and horizontal cores with short range (weak spatial continuity).
- Eu-154: Relatively higher variability along the horizontal core, which might be due to location of horizontal core.
- Eu-155: Maximum variability along the horizontal core (probably due to its location), and the minimum variability along the channels.

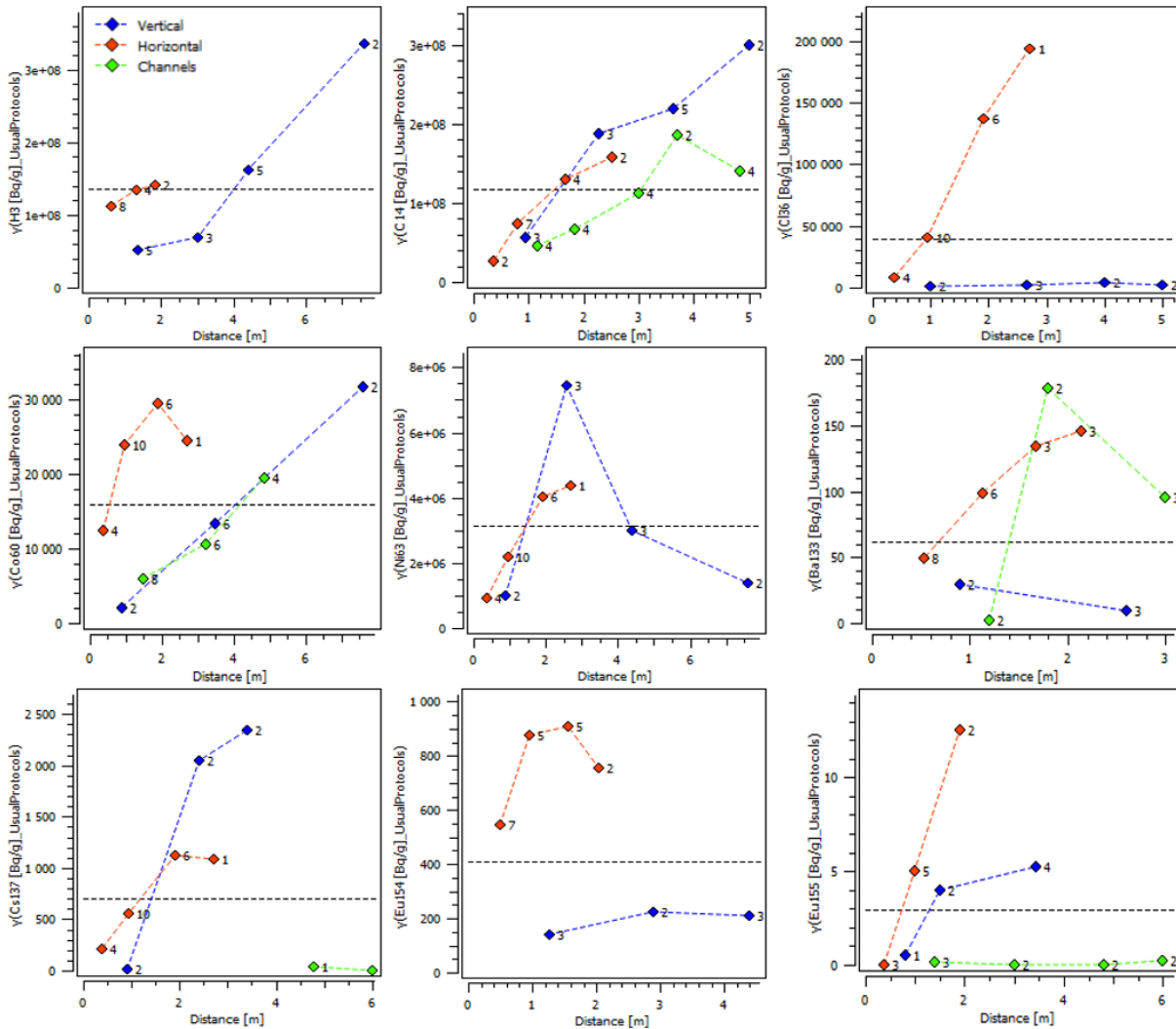


Figure 24. Experimental variograms of nine radionuclides in the graphite of G2 reactor.

Variogram modelling is done for C-14, which has the greatest number of sample pairs, and the most conformable experimental variograms. The spatial variability of C-14 activity is the same along vertical and horizontal (azimuth of 76.15°) cores. While it is observed that the spatial variability is much lower along the channels (azimuth of 166.15°). A spherical anisotropic function with no nugget effect is fitted to the experimental variogram, considering longer continuity (range) along the channels (Figure 25).

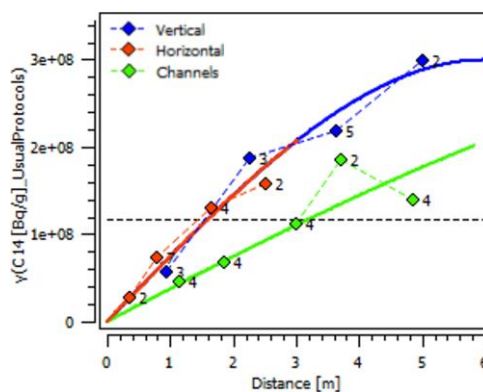


Figure 25. Variogram modelling of C-14 activity in the graphite of G2 reactor. Anisotropic spherical function is used.

1.2.4.4 Dispersion analysis by variogram

In Chapter 1.2.2.6, dispersion analysis was done for all radionuclides, using coefficient of variation, which is a classical statistical quantity for that purpose. In this chapter, dispersion analysis of C-14 is then done using variography analysis. Variogram is the averaged variance of data couples at different distances (Eq. 1). So, by distinguishing the distances between duplicates, subsamples and samples, variance dispersion can be visualized from duplicates to subsamples and to samples, using experimental variogram.

$$\gamma(h) = \frac{1}{2N^2} \sum_{|x_i - x_j| \approx h} (x_i - x_j)^2 \tag{Eq. 1}$$

Where *N* is the number of points (so *N*² is the number of pairs)

Sample locations were reported in the database while no information regarding subsamples or duplicates locations. So, subsamples were artificially considered as equally distributed within each sample, and duplicates size was considered to be one millimetre in the middle of each subsample (Figure 26). So, the distance between two adjacent duplicates is one millimetre, and the distance between adjacent subsamples is about 30 mm. Worthy to mention that no duplicate exists in the channels where subsamples are 20 mm apart.

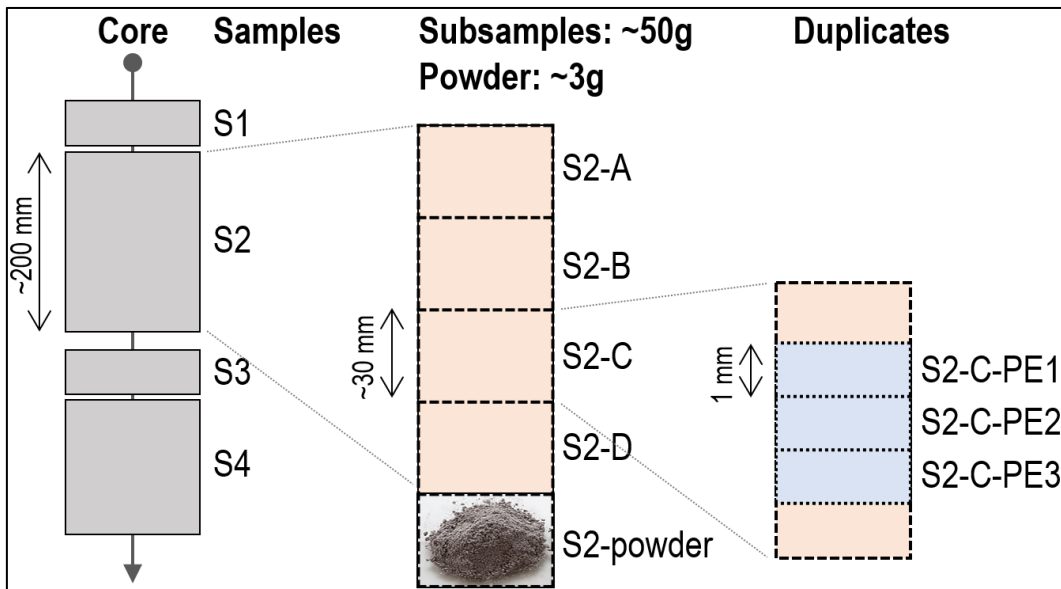


Figure 26. Sampling, subsampling and duplicate analysis.

Duplicates date was corrected to the 1st January 2016 to be homogeneous in statistical and geostatistical analyses. Separately in each core, the average of duplicates variances and subsamples variances were calculated and compared to the variance of samples (Table 5). The variance increases from duplicates to subsamples and to samples (Figure 27), as has shown previously in the Chapter 1.2.2.6.

Table 5. Dispersion of average of variances.

	Duplicates	Subsamples	Samples
Vertical	1'187'794	4'001'330	172'457'785
Horizontal	157'168	2'675'125	85'459'208
Channels	--	16'558'826	90'814'444

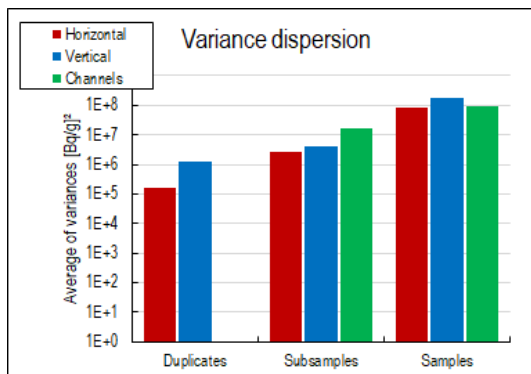


Figure 27. Variance dispersion of C-14.

Then, the full duplicate dataset was imported (Figure 28). Besides, a weight was attributed to each duplicate, according to the corresponding subsample mass. The sum of duplicate weights within each sample is equal to one. This weight compensates the mass difference between the subsamples.

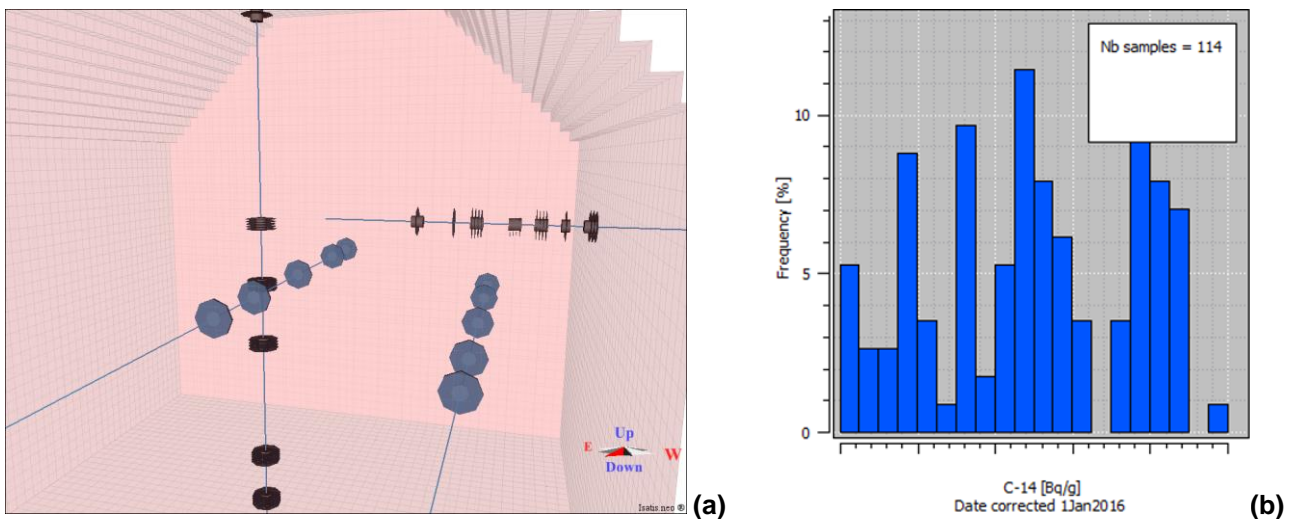


Figure 28. Imported duplicates and samples (a) and histogram of duplicates (b).

C-14 duplicates experimental variogram (Figure 29) looks like sample variogram (Figure 25). For the distances greater than one meter, both the variograms are the same, however the duplicate-based variogram is more detailed at the origin (small distances), and provides some information about nugget effect and slope at the origin of the variable. Besides, more couples are participated in calculating the duplicate-based variogram. The nugget effect on the variogram of Figure 29, was calculated the average of variances of duplicates and subsamples in Table 5. Also, samples variance of Table 5 correspond to the sill of the variograms of Figure 29.

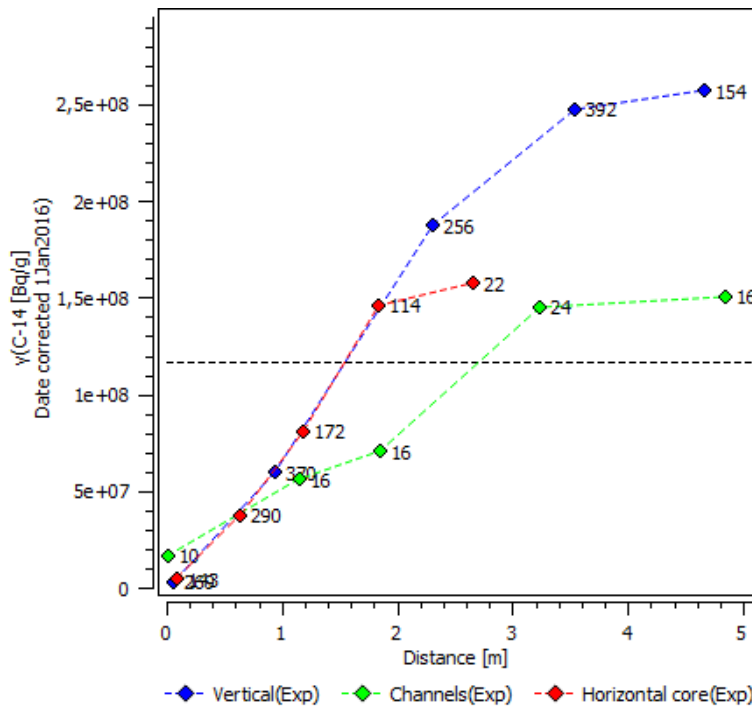


Figure 29. Directional experimental variograms of C-14 duplicates.

1.2.5 Postprocessing with spatial structure (geostatistics)

Still for confidentiality reasons, the real activity levels are hidden. To be able to present accumulation curves, an arbitrary unit is used and presented as XBq (such as kBq, MBq, GBq...). Thus relative comparison are consistent but absolute values remains confidential.

1.2.5.1 Carbon-14 probabilistic characterization

Having too limited number of available samples and lack of a representative sampling coverage, C-14 activity is not recommended for simple interpolation inside the G2 reactor graphite (most of the domain under extrapolation). However, a probabilistic study based on geostatistical simulation can differentiate high- and low-risk areas in the graphite as well as total accumulation (radiological inventory). In this regard, Turning Bands Simulation (TBS) was applied to generate 1000 realizations of C-14 values within the graphite (back reflector is exempted since no sample).

Accordingly, the accumulation (inventory) of C-14 is calculated using Eq. 2.

$$Acc = Vol \times Ave \times Den \times c \tag{Eq. 2}$$

Where:

- Vol , in m^3 , is the graphite volume;
- Ave , in $\frac{Bq}{g}$, is the average of C-14 activity for each realization;
- $Den = 1.69 \times 10^6 \frac{g}{m^3}$ is the density of graphite [3]; and
- $c = 0.95$, is a unitless correction of density, considering 9.6% porosity in the moderator (designed for the channels) and the volume proportion of moderator in the graphite without back reflector (54%).

The accumulation (inventory) of C-14 varies from 15 XBq at minimum to 35 XBq at maximum as presented on Figure 30. More robustly, the median value (Q50) is 23.9 XBq with a 90% confidence interval between 18.7 and 29.6 XBq.

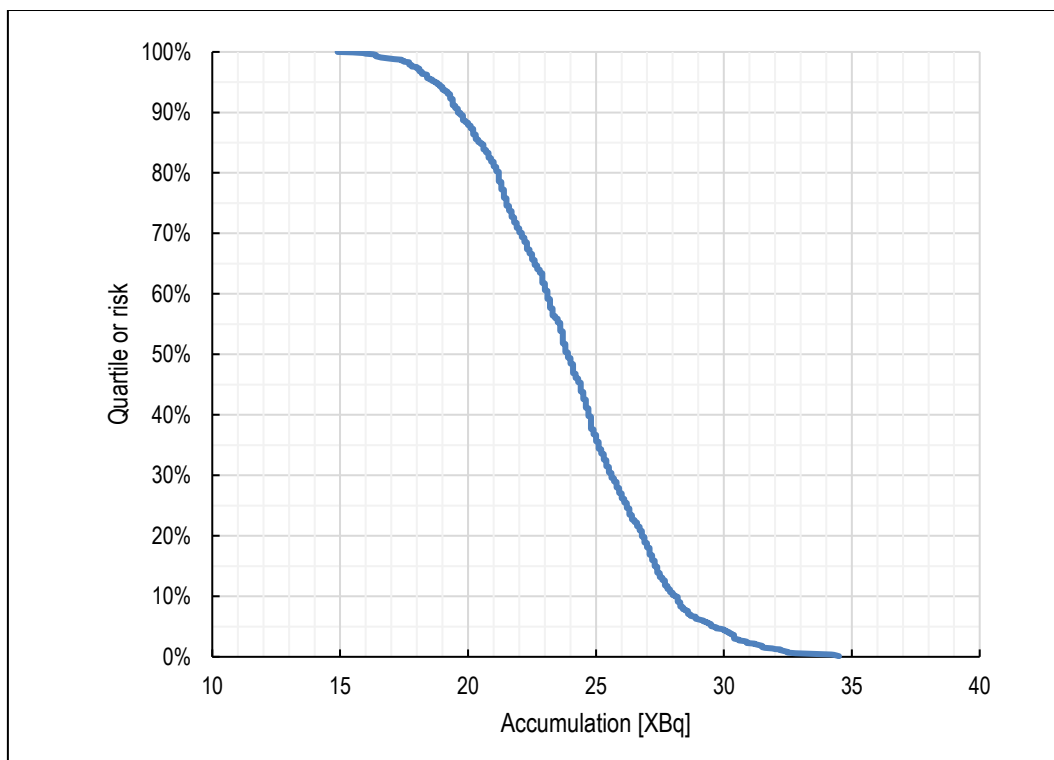
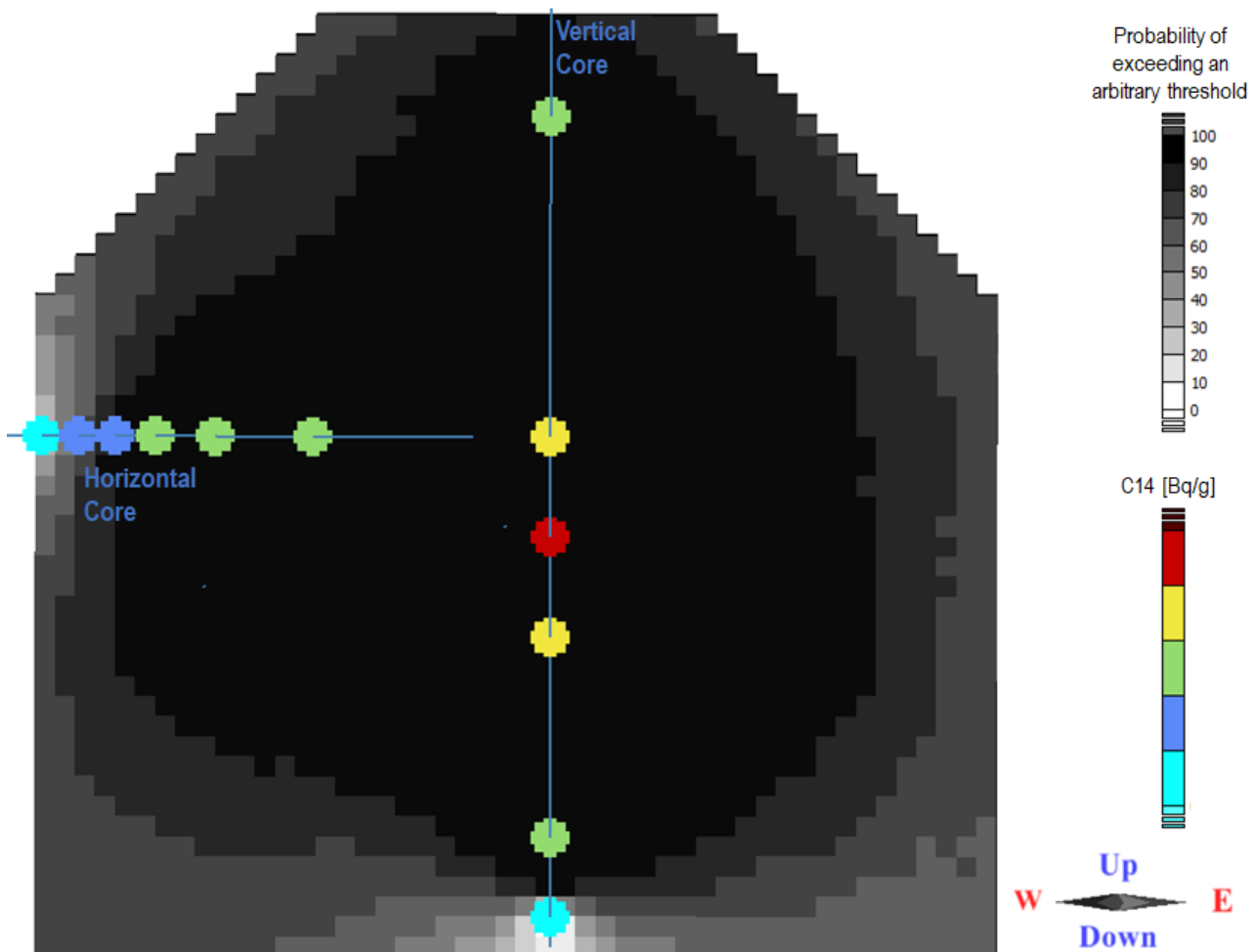


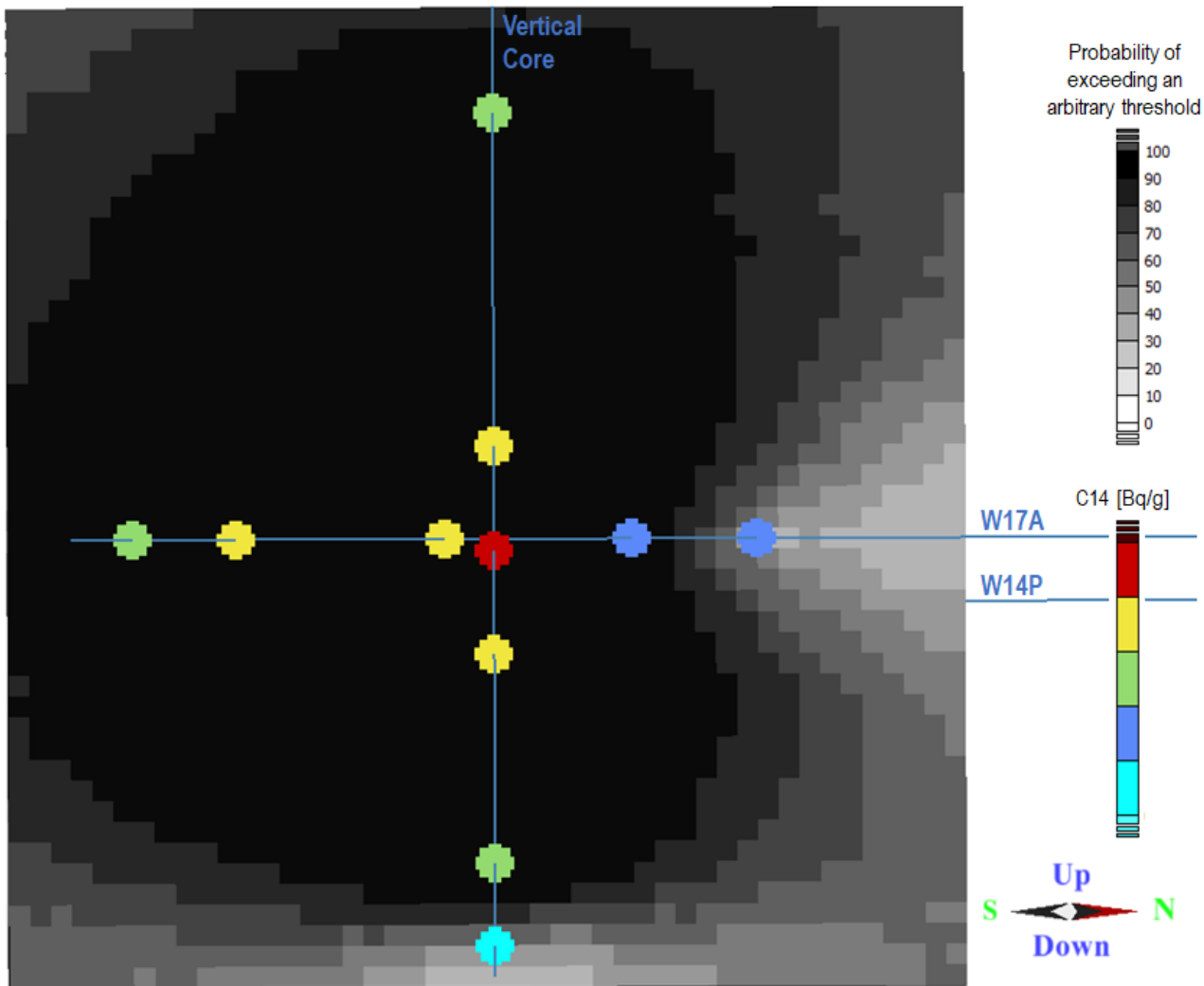
Figure 30. Accumulation (inventory) of C-14.

The realizations were then used to calculate the local probability of exceeding an arbitrary threshold for C-14, in the cells of the estimation grid (Figure 31ab). Consequently, the cells with the probability of higher than 95% were plotted (Figure 31c). For the real classification, probability around 20-30 % would be more adequately selected.



(a)

Isatis neo ®



Isatis.neo®

(b)

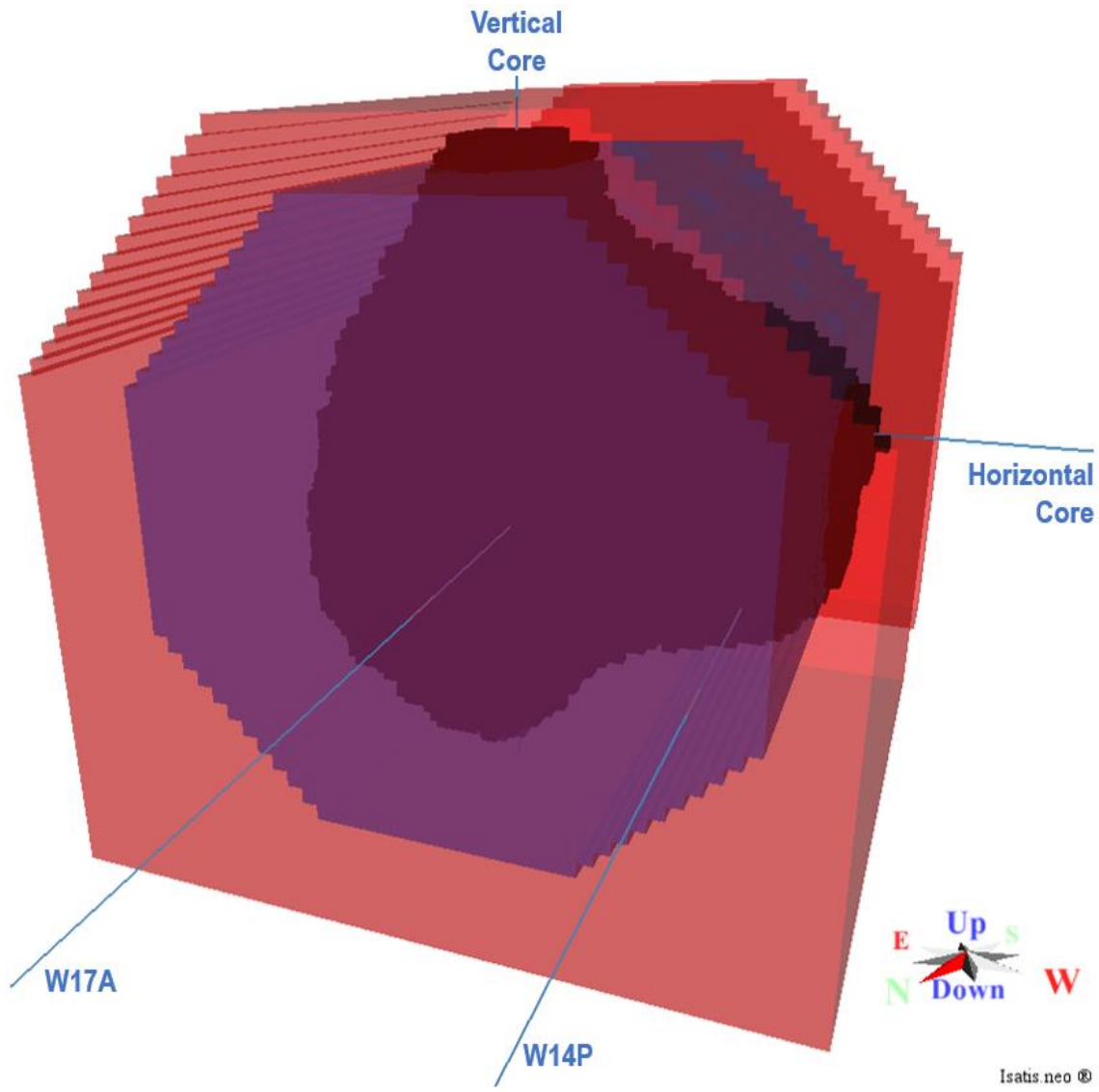


Figure 31. Local risk of C-14 in the graphite of G2 reactor. Probability of exceeding an arbitrary chosen threshold for C-14: a) Vertical East-West section at the location of about the vertical core. b) Vertical North-South section at location of about the vertical core. c) 3D view of cells with 95% probability of exceeding the arbitrary threshold of C-14.

The information of local risk (Figure 31) could be synthesized and presented as a global classification curve (Figure 32). Depending on the accepted risk (vertical axis), the graphite volume where C-14 exceeds the arbitrary threshold may vary from 400 m³ at minimum to 745 m³ at maximum (variation >80%).

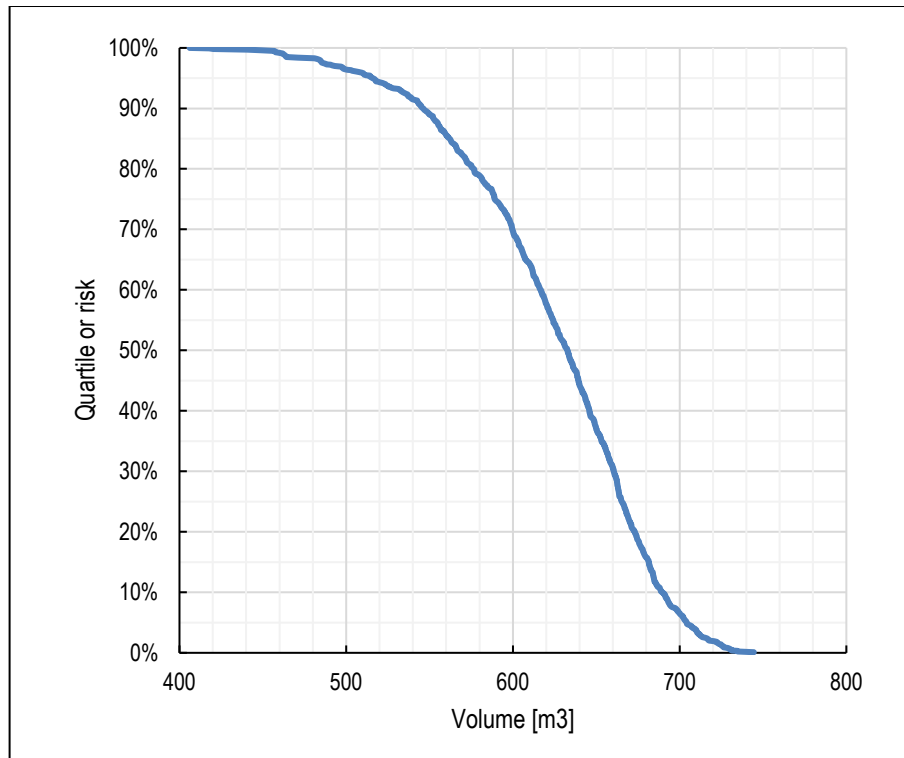


Figure 32. Classification curve of graphite volumes from G2 reactor with activity higher than the arbitrary chosen threshold of C-14.

1.2.5.2 Carbon-14 multivariable characterization

Regression-based model of carbon-14

In the moderator of graphite core, the horizontal core is parallel to the axis IX (azimuth of 76.15°), the channels W17A and W14P are parallel to the axis IY (azimuth of 166.15°), and the vertical core is parallel to the axis IZ (Figure 33). The radius r is defined on the plane XZ with the reference in the middle of the graphite face, i.e. IX=24.5 and IZ=22.

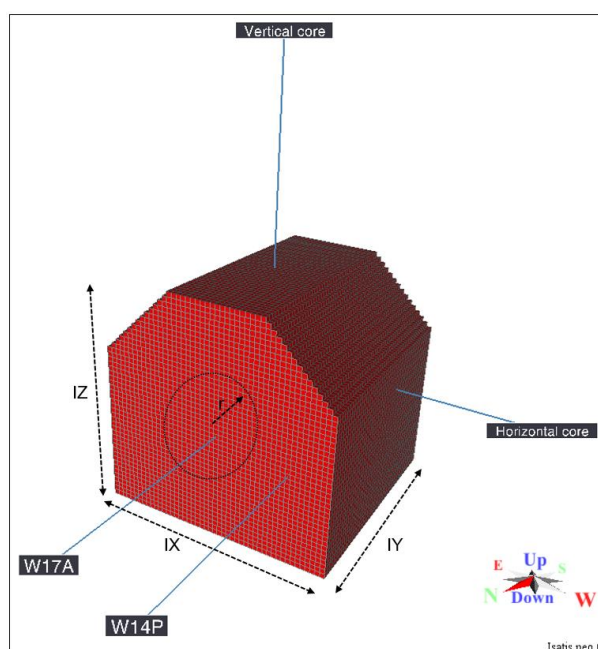


Figure 33. Grid blocks of moderator of graphite. Back reflector is ignored.

So, variability of C-14 along each core could be assigned to corresponding axis. Along IX, IY and IZ axis, variability of C-14 is modelled by second degree regression method, while linear model is used along r. The regression model based on r contains the information of the regression models based on IX and IZ.

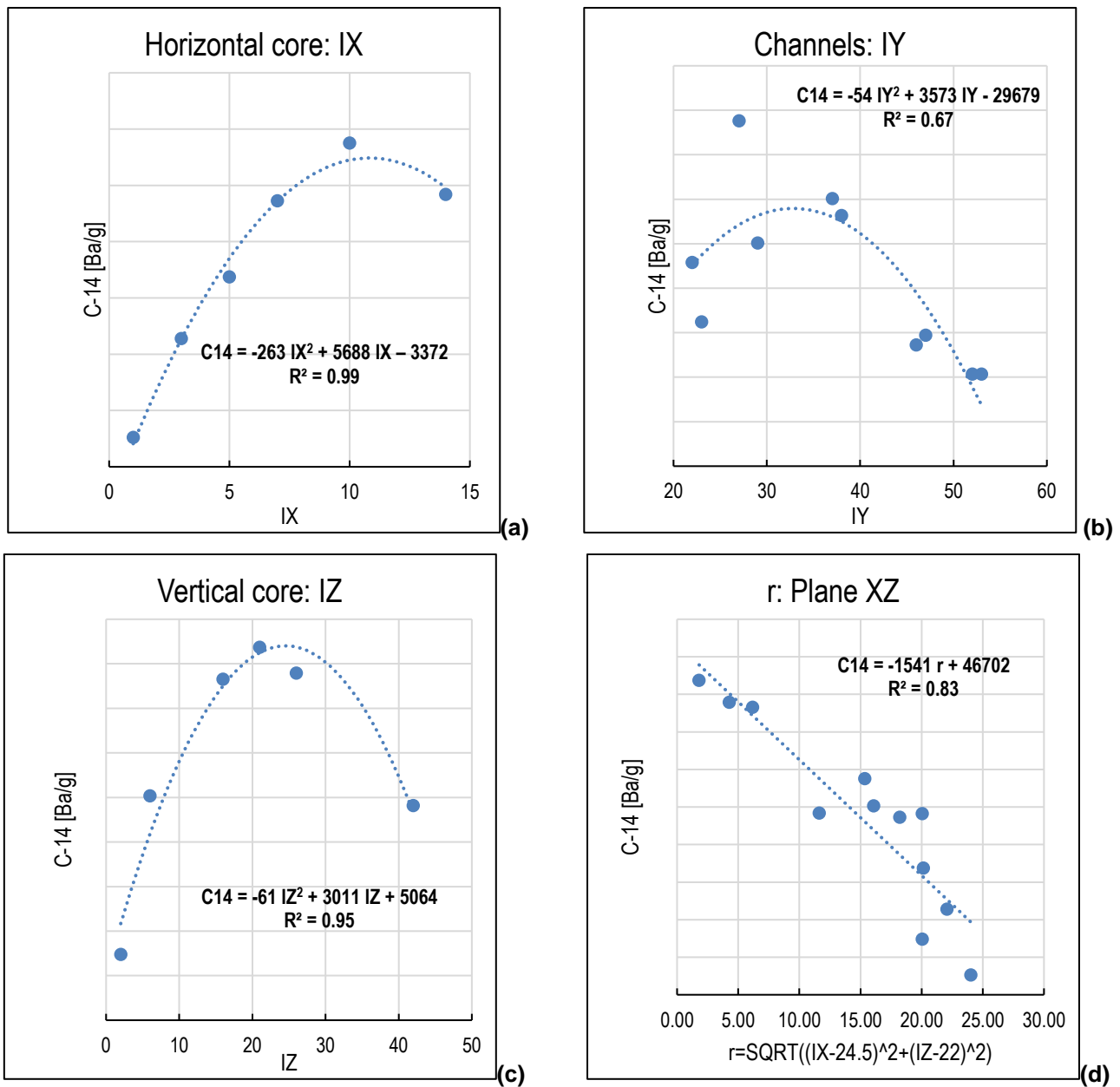


Figure 34. Variability of C-14 in different directions, modelled by regression models.

Then, based on two regression models IY and r, the value of C-14 is estimated at each grid block of the moderator. The C-14 estimation is done in four steps (Figure 35):

- (i) r-based regression model is calculated at each grid block.
- (ii) IY-based regression model is calculated at each grid block.
- (iii) The output of IY regression model is normalised to become unitless, and to be used as normalizer of the output of r regression model along the IY axis.
- (iv) The output of r regression model and unitless IY regression model are multiplied.

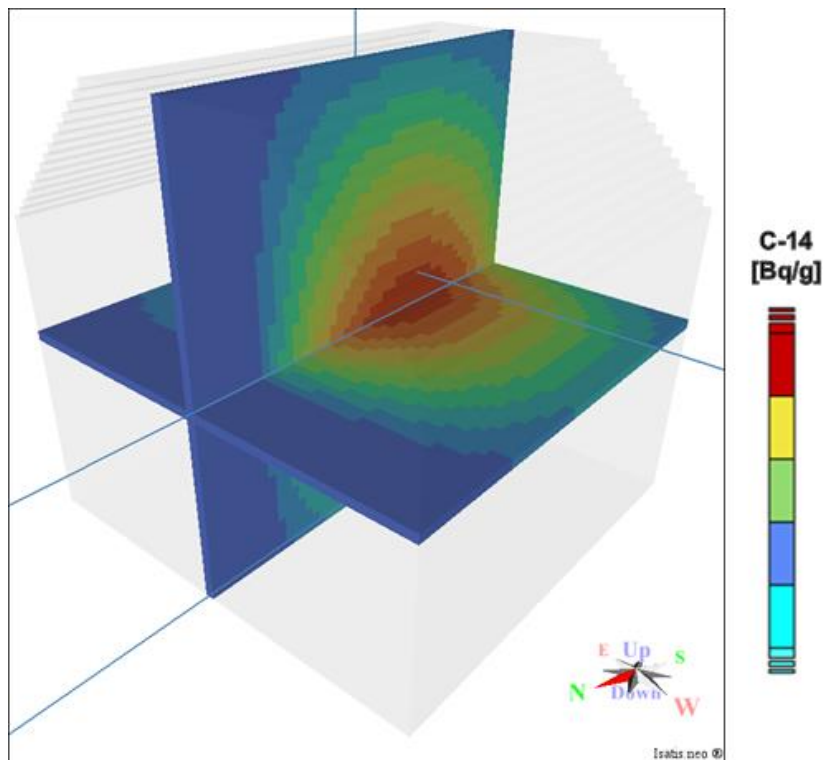


Figure 35. Regression-based model of C-14 in the moderator of graphite core.

The regression-based model of C-14 is compared to the core-based C-14, revealing high correlation between them (Figure 36).

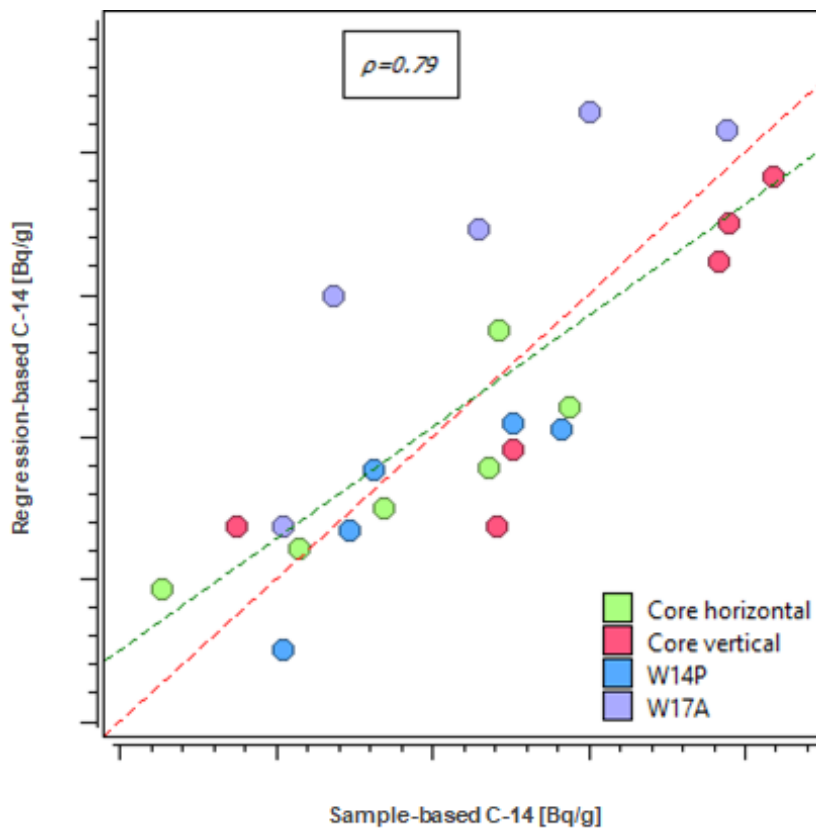


Figure 36. Cross-plot of regression-based C-14 versus sample-based C-14.

Co-simulation of carbon-14

Co-simulation is a multivariate geostatistical analysis generating realizations of a variable, (here C-14) based on a principal variable (C-14 in samples), and an auxiliary variable (regression-based C-14). The advantage of co-simulation to univariable classical simulation is conditioning the realizations to an auxiliary variable which has a better coverage than the principal variable. If the auxiliary variable is available at all the target points (grid blocks), collocated co-simulation could be applied. In this example, the auxiliary variable (regression-based C-14) is already calculated and available at all the grid blocks.

The principal and auxiliary variables must be correlated (Figure 36), and the correlation coefficient is used for creating a cross-variogram based on previously modelled simple variogram (Figure 25). Principle variable, auxiliary variable and cross-variogram were used in Turning Bands Co-simulation (TBS co-simulation) to generate 1000 realizations, and to calculate probability of exceeding the same arbitrary threshold (sections on right, Figure 37). The sections on left are simulation results already presented on Figure 31. They are included here to compare the results visually: In the borders, the probability of exceeding the threshold is decreased considerably in the co-simulation-based analysis.

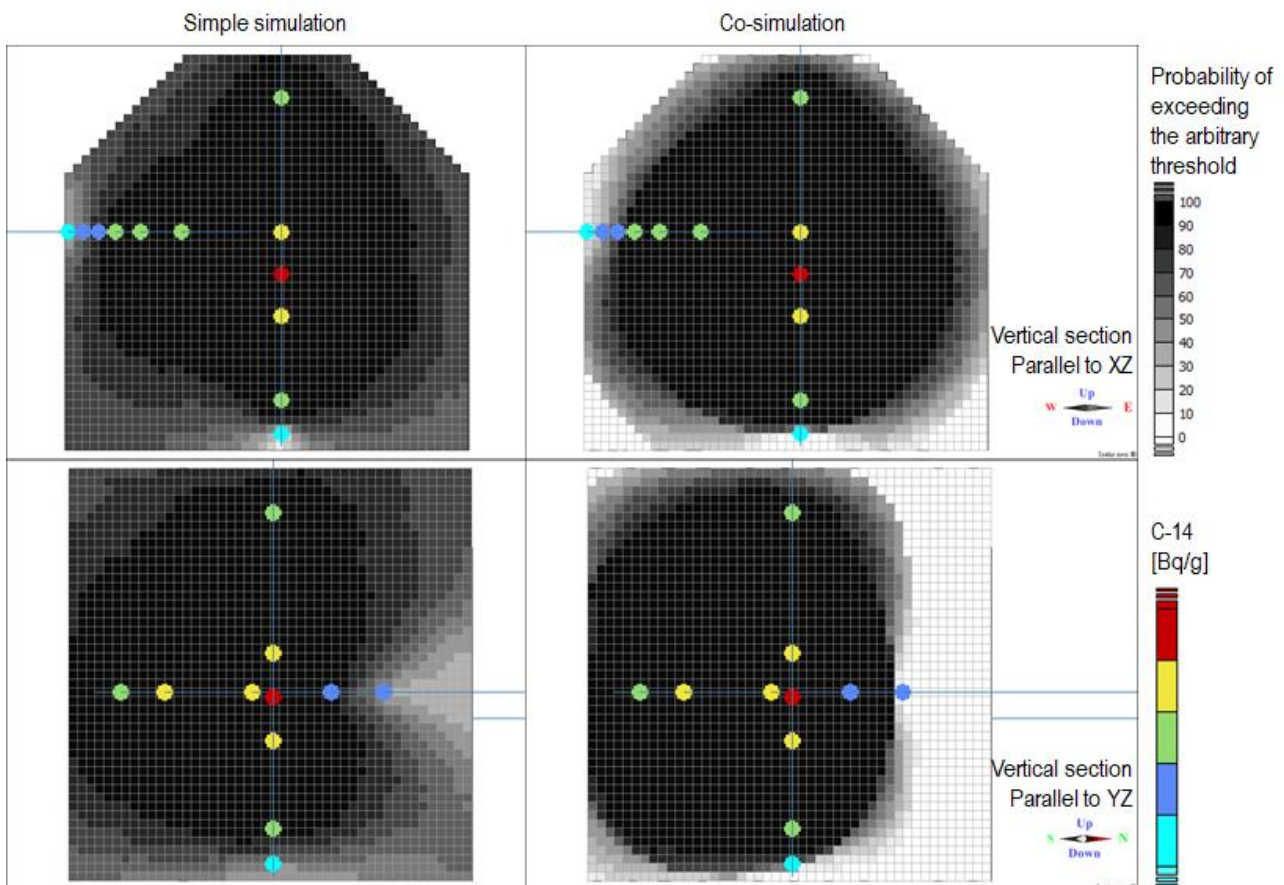


Figure 37. Local risk of C-14 in the graphite of G2 reactor. Probability of exceeding the selected threshold, calculated by simple simulation (two sections on left) and co-simulation (two sections on right). The main variable (C-14 samples) are also shown.

In order to further analyse the outputs of simulation and co-simulation, the histograms of the probability of exceeding the threshold (simulation and co-simulation) are compared. Simulation-based results (Figure 38a) show more intermediate uncertain values (probabilities of around 70%), while co-simulation-based results (Figure 38b) show more end-member certain values (probabilities around zero or 100%). The cross-plot of the simulation versus co-simulation probabilities reveal that simulation-based results are overestimation compared to simulation values (Figure 38c).

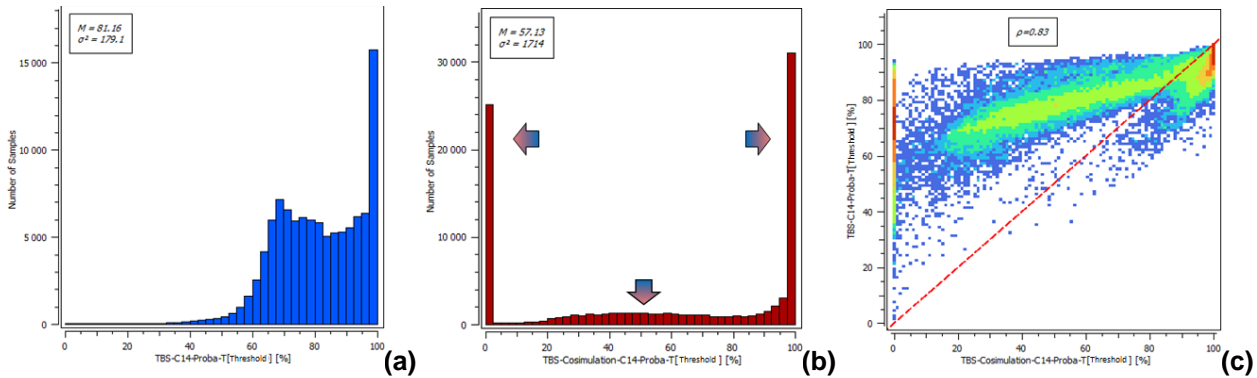


Figure 38. Histograms of probability of exceeding the threshold, calculated by simulation (a) and co-simulation (b), and cross-plot of them (c).

Risk analysis followed by co-simulation

The information of local risk (Figure 37) is synthesized and presented as the global risk (Figure 39). Depending on the accepted risk (vertical axes of Figure 39ab), the graphite volume where C-14 exceeds the selected threshold may vary from 330 m³ at minimum to 520 m³ at maximum (variation=58%), according to the co-simulation curve while the volume variation according to simple simulation curve (TBS) is >80%, Figure 39a.

Accordingly, the accumulation (inventory) of C-14 is calculated using Eq. 2. The accumulation (inventory) of C-14, higher than the selected threshold varies from 13 XBq at minimum to 22 XBq at maximum (variation=69%), compared to >130% on the simple simulation curve (TBS), Figure 39b.

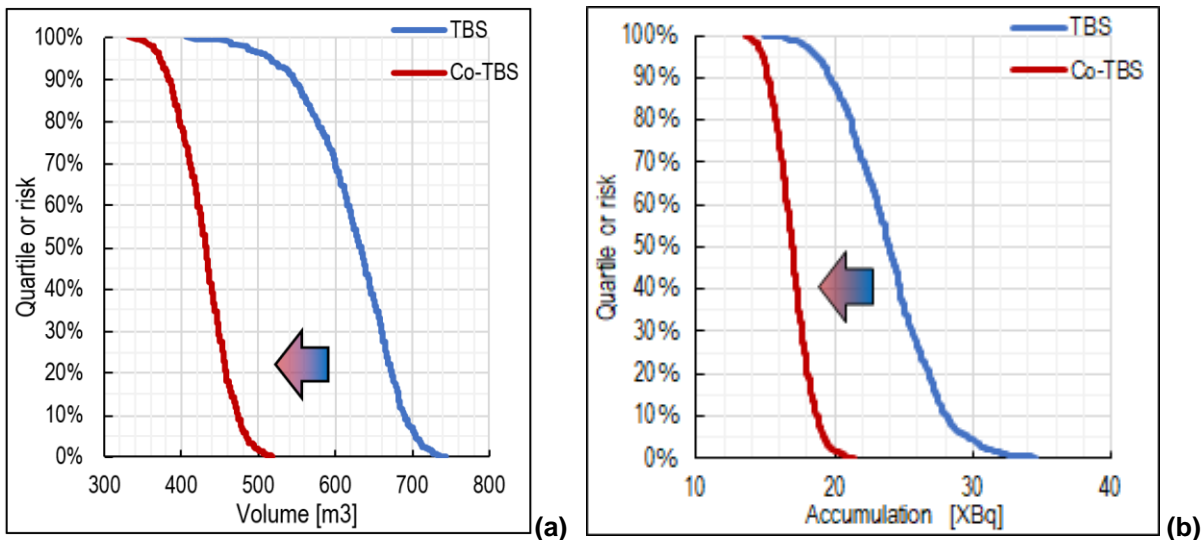


Figure 39. Global risk of C-14 in the graphite of G2 reactor: a) Volume of the graphite of G2 reactor with activity higher than the selected threshold for C-14. b) Accumulation (inventory) of C-14. The curves of simple simulation (TBS) and co-simulation (Co-TBS) are compared.

Hence, using multivariate geostatistics, range of estimated waste volume and inventory are reduced, i.e. more certainty in the decision-making. Considering some accepted risks, the graphite volume and C-14 inventory is read and reported in Table 6 and 4, using simple and co-simulation.

Table 6. Graphite volume, exceeding the selected threshold for C-14, corresponding to the accepted risk (Figure 39a).

Accepted risk	Simple simulation	Co-simulation
Q10%	546 m ³	385 m ³
Q25%	589 m ³	405 m ³
Q50%	633 m ³	432 m ³
Q75%	665 m ³	454 m ³
Q90%	690 m ³	475 m ³

Table 7. Inventory of C-14 corresponding to the accepted risk (Figure 39b).

Accepted risk	Simple simulation	Co-simulation
Q5%	19 XBq	15 XBq
Q50%	24 XBq	17 XBq
Q95%	30 XBq	19 XBq

1.2.6 Is the objective achieved?

The radiological inventory can be computed using three different data processing techniques:

- Direct spatial fitting
- Through the spatial correlation (variogram) for certain nuclides (C-14 for instance)
- Through multivariate spatial correlation to integrate a spatial fitting to reduce estimation uncertainties.

They show comparable results due to the good spatial continuity of the activation phenomenon even if the number of data is quite limited.

In addition, the databased proved to be richer than expected with the presence of measurement repetitions, subsamples and samples along 4 cores (not to mention specific analysis methods for Tritium). **These numerous data analyses enable a very interesting dispersion decomposition at the different levels.**

1.2.7 Sampling design

Sampling recommendations are then driven by the characterisation objectives. For total inventory, additional data in unsampled areas are expected not to impact significantly the total activity as most activated parts are already sampled and contribute the most to the output result but improvement on uncertainty may be found (risk curves become more vertical). Using more precise waste classification criteria for the different nuclides (long-lived, reference activity levels), some specific areas in the graphite block may be pointed out for additional investigations. However, the use of a sound activation model may serve as efficiently (if not more) as additional data as seen in § 1.2.5.2.

1.3 References

- [1] Pradelle, M. 2008. Historique de fonctionnement réacteurs G2 G3. *Commissariat à l'énergie atomique (CEA)*. NOTE TECHNIQUE MAR/DPAD/2008.
- [2] Comte, J. 2016. État des connaissances sur les graphites des réacteurs G2/G3. *Commissariat à l'énergie atomique (CEA)*. NOTE TECHNIQUE CEA/DEN/CAD/DEC/SA3C/LARC/NT/16-003-Indice 0.



- [3] Van Lauwe, A. 2016. Calcul d'activation des graphites du réacteur G2. *Commissariat à l'énergie atomique (CEA)*. NOTE TECHNIQUE CEA/DEN/DANS/DM2S/SERMA/LPEC/NT/16-6015/A-DR.